The Astrophysical Journal, 728:109 (21pp), 2011 February 20 doi:10.1088/0004-637X/728/2/109

N-BODY SIMULATIONS FOR EXTENDED QUINTESSENCE MODELS

Baojiu Li[1,2], David F. Mota[3], and John D. Barrow[2]
[1] DAMTP, Centre for Mathematical Sciences, University of Cambridge, Wilberforce Road, Cambridge CB3 0WA, UK; b.li@damtp.cam.ac.uk
[2] Kavli Institute for Cosmology Cambridge, Madingley Road, Cambridge CB3 0HA, UK; j.d.barrow@damtp.cam.ac.uk
[3] Institute of Theoretical Astrophysics, University of Oslo, 0315 Oslo, Norway; d.f.mota@astro.uio.no
Received 2010 September 7; accepted 2010 December 14; published 2011 January 26

ABSTRACT

We introduce the *N*-body simulation technique to follow structure formation in linear and nonlinear regimes for the extended quintessence models (scalar–tensor theories in which the scalar field has a self-interaction potential and behaves as dark energy), and apply it to a class of models specified by an inverse power-law potential and a non-minimal coupling. Our full solution of the scalar field perturbation confirms that, when the potential does not change strongly on perturbation, the effects of the scalar field can be accurately approximated as a modification of background expansion rate plus a rescaling of the effective gravitational constant relevant for structure growth. For the models we consider, these have opposite effects, leading to a weak net effect in the linear perturbation regime. However, on the nonlinear scales the modified expansion rate dominates and could produce interesting signatures in the matter power spectrum and mass function, which might be used to improve the constraints on the models from cosmological data. We show that the density profiles of the dark matter halos are well described by the Navarro–Frenk–White (NFW) formula, although the scalar field could change the concentration. We also derive an analytic formula for the scalar field perturbation inside halos assuming an NFW density profile and sphericity, which agrees well with numerical results if the gravitational potential parameter is appropriately tuned. The results suggest that for the models considered, the spatial variation of the scalar field (and thus the locally measured gravitational constant) is very weak, and so local experiments could see the background variation of the gravitational constant.

Key words: cosmology: miscellaneous – dark energy – gravitation – large-scale structure of universe – methods: numerical

Online-only material: color figures

1. INTRODUCTION

The nature of the dark energy (Copeland et al. 2006) is one of the most difficult challenges facing physicists and cosmologists now. Although a cosmological constant (plus cold dark matter, to provide the concordance ΛCDM paradigm) could be a solution (and is indeed consistent with virtually all current observations), it suffers from theoretical difficulties such as why its value must be so small yet nonzero, and why it becomes dominant only at the low redshift. In all the alternative proposals to tackle this problem, a quintessence scalar field (Zlatev et al. 1999; Wang et al. 2000) is perhaps the most popular one (although a new proposal by Barrow & Shaw 2010 provides a completely new type of explanation that does not require new scalar fields). In such models, the scalar field φ is slowly rolling down its potential, its energy density is dominated by the potential energy and almost remains constant provided that the potential is flat enough. The flatness of the potential, however, means that the mass of the scalar field is in general very light and as a result the scalar field almost does not cluster so that its effects on cosmology are mainly on the (modified) background expansion rate.

One reason for the wide interest in quintessence models is that scalar fields appear in abundance in high-energy physics theories, in which they are often coupled to the curvature invariants or even other matter species, leading to the so-called extended quintessence (Perrotta et al. 2000; Baccigalupi & Perrotta 2000; Perrotta et al. 2000) and coupled quintessence (Amendola 2000, 2004; Jesus et al. 2008) models, respectively. The former is just a special class of a scalar–tensor theory (Fujii & Maeda 2003; Riazuelo & Uzan 2002), with the scalar field being the dark energy. These two classes of generalized quintessence models have been studied in detail in the linear regime in the literature (Uzan 1999; Bartolo & Pietroni 1999; Bean 2001; Bean & Magueijo 2001; Mangano et al. 2003; Clifton et al. 2005; Nunes & Mota 2006; Pettorino et al. 2005; Koivisto 2005; Brookfield et al. 2006; Schimd et al. 2005; Koivisto & Mota 2007; Mota & Shaw 2007, 2006; Lee et al. 2006; Mota et al. 2007; Bean et al. 2008a, 2008b; Boehmer et al. 2008, 2010).

In recent years, studies of the cosmological behavior of the coupled quintessence model in the nonlinear regime have also been made, either via semi-analytical methods (Manera & Mota 2006; Mota & van de Bruck 2004; Mota 2008; Shaw & Mota 2008; Mota et al. 2008a, 2008b; Saracco et al. 2010; Wintergerst & Pettorino 2010), or using *N*-body simulation techniques (Maccio et al. 2004; Nusser et al. 2005; Kesden & Kamionkowski 2006a, 2006b; Springel & Farrar 2007; Farrar & Rosen 2007; Baldi & Pettorino 2010; Hellwing & Juszkiewicz 2009; Keselman et al. 2009, 2010; Hellwing et al. 2010; Baldi 2010; Baldi et al. 2010). In these studies, the effect of the scalar field is generally approximated by a Yukawa-type "fifth force" or by a rescaling of the gravitational constant or the particle mass, without solving the scalar field equation explicitly. Very recently, Li & Zhao (2009, 2010), Zhao et al. (2010b), and Li & Barrow (2011) gave a new treatment and obtained an explicit solution to the scalar field perturbation on a spatial grid. The new results confirmed that the approximations adopted in the old literature were good for the models considered there (where the scalar potential was not very nonlinear), but for highly nonlinear potentials they broke down.

For the extended quintessence (more generally scalar–tensor) models, investigations using N-body simulations are rarer. The work of Pettorino & Baccigalupi (2008), for example, outlined a recipe that uses certain approximation, such as a rescaling of the gravitational constant, and does not solve the scalar field equation of motion explicitly; this algorithm has recently been used by De Boni et al. (2010). In Rodriguez-Meza et al. (2007) and Rodriguez-Meza (2008a, 2008b), the authors approximated the effect of scalar field coupling as a Yukawa force. However, none of these previous works try to solve the scalar field on a mesh directly, and this is the purpose of this work.

The aims of this work are threefold. First, we want to develop the formulae and methods that are needed to solve the scalar field explicitly, which could serve as the basis for future work, and to find the regime of validity of our method. Second, we want to understand whether or not the approximations adopted in the previous studies are good; given the severe limits on the computing power, if those approximations do work well, then one does not need to resort to a less-economical exact scalar field solver. Finally, we want to study structure formation in the nonlinear regime for some specific models, and investigate both the scalar field effects on the clustering of matter and the spatial variation of the gravitational constant (which is common to scalar–tensor theories).

The organization of this paper is as follows. In Section 2, we list the basic equations that are needed in N-body simulations and give their respective non-relativistic limits. Some useful expressions are listed in Appendix A, and the discrete versions of the resulting equations are discussed and summarized in Appendix B. In Section 3, we briefly describe the numerical code we are using (relegating further details to Knebe et al. 2001 and Li & Zhao 2010) and the physical parameters of our simulations. We also present some results regarding the background cosmology and linear perturbation evolution in our models, which could be helpful in the understanding of the N-body simulation results (our algorithm for the background cosmology is summarized in Appendix C). Section 4 contains the N-body simulation results, including key structure formation observables such as the nonlinear matter power spectrum, mass function, and dark matter halo profile, as well as the spatial variation of the scalar field. It also includes several checks of the approximations made in the literature. We finally summarize and conclude in Section 5.

We use the unit $c = 1$ unless explicitly restoring c in the equations. The metric convention is $(+, -, -, -,)$. Indices $a, b, c, \ldots$ run $0, 1, 2, 3 \ldots$, while $i, j, k, \ldots$ run $1, 2, 3 \ldots$.

2. THE EQUATIONS

This section presents the equations that will be used in the N-body simulations, the model parameterization, and discretization procedure for the equations.

2.1. The Basic Equations

We consider a general Lagrangian density for scalar–tensor theories:

$$\mathcal{L} = \frac{1}{2\kappa_*}\left[1 + f(\varphi)\right] R - \frac{1}{2}\nabla^a\varphi\nabla_a\varphi + V(\varphi) - \mathcal{L}_f, \quad (1)$$

in which $\kappa_* = 8\pi G_*$ where G_* is the (bare) gravitational constant, R is the Ricci scalar, $f(\varphi)$ is the coupling function between the scalar field φ and curvature, $V(\varphi)$ the potential for φ, and $\mathcal{L}_f$ the Lagrangian density for fluid matter (baryons, photons, neutrinos, and cold dark matter). Note that G_* is a fundamental constant of the theory.

Varying the associated action with respect to metric g_{ab} yields the energy–momentum tensor of the theory (note the tilde, which is used to distinguish it from the $T_{\rm ab}$ defined below):

$$\tilde{T}_{\rm ab} = T^f_{\rm ab} + \nabla_a\nabla_b\varphi - \frac{1}{2}g_{\rm ab}\nabla^c\varphi\nabla_c\varphi + g_{\rm ab}V(\varphi) - \frac{1}{\kappa_*}[f(\varphi)G_{\rm ab} + (g_{\rm ab}\nabla^c\nabla_c - \nabla_a\nabla_b)f(\varphi)], \quad (2)$$

where $G_{\rm ab} = R_{\rm ab} - \frac{1}{2}g_{\rm ab}R$ is the Einstein tensor, and $T^f_{\rm ab}$ is the energy–momentum tensor for matter (including baryons, dark matter, neutrinos, and photons, which we collectively refer to as "fluid matter," although in N-body simulations we use discrete particles rather than a fluid).

As usual, we can rearrange the Einstein equation as

$$G_{\rm ab} = \kappa_*\tilde{T}_{\rm ab} \quad (3)$$

so that it now looks like

$$G_{\rm ab} = \frac{\kappa_*}{1+f}T^f_{\rm ab} - \frac{1}{1+f}(g_{\rm ab}\nabla^c\nabla_c - \nabla_a\nabla_b)f + \frac{\kappa_*}{1+f}\left[\nabla_a\varphi\nabla_b\varphi - \frac{1}{2}g_{\rm ab}(\nabla\varphi)^2 + g_{\rm ab}V\right] \equiv \kappa_*T_{\rm ab}. \quad (4)$$

Note the difference between $T^f_{\rm ab}$ and $T_{\rm ab}$; throughout this paper, we will use a superscript ^{f} for normal fluid matter, and quantities without a superscript ^{f} always mean the total effective ones (the final line of Equation (4)). It is sometimes useful to define an effective Newton constant $\kappa_{\rm eff} \equiv \kappa_*/(1+f)$. Neither κ_* nor $\kappa_{\rm eff}$ is the gravitational constant measured in a Cavendish-type experiment, which we denote instead by $\kappa_\oplus$ and is derived by Damour & Esposito-Farese (1992) in the post-Newtonian limit for weakly self-gravitating, slow-moving, and weakly internally stressed bodies as

$$\kappa_\oplus = \frac{\kappa_*}{1+f}\frac{2 + 2f + 4\left(\frac{df}{d\sqrt{\kappa_*}\varphi}\right)^2}{2 + 2f + 3\left(\frac{df}{d\sqrt{\kappa_*}\varphi}\right)^2}, \quad (5)$$

where $\sqrt{\kappa_*}$ is added to make $\sqrt{\kappa_*}\varphi$ dimensionless, which is the convention we always follow below. $\kappa_\oplus$ itself is obviously not a constant and we measure only its present day value, $\kappa_{\oplus 0}$.

Varying the action with respect to the scalar field, φ, gives the scalar field equation of motion

$$\nabla^a\nabla_a\varphi + \frac{\partial V(\varphi)}{\partial\varphi} + \frac{R}{2\kappa_*}\frac{\partial f(\varphi)}{\partial\varphi} = 0. \quad (6)$$

Since we will follow the motions of dark matter particles in the N-body simulations, so we also need their geodesic equation. The dark matter Lagrangian for a point particle with mass m_0 is

$$\mathcal{L}_{\rm CDM}(\mathbf{y}) = -\frac{m_0}{\sqrt{-g}}\delta(\mathbf{y} - \mathbf{x}_0)\sqrt{g_{ab}\dot{x}^a_0\dot{x}^b_0}, \quad (7)$$

where $\mathbf{y}$ is the general coordinate denoting an arbitrary point in the space and $\mathbf{x}_0$ is the coordinate of the center of the particle. From this equation we derive the corresponding energy–momentum tensor

$$T^{\rm ab}_{\rm CDM} = \frac{m_0}{\sqrt{-g}}\delta(\mathbf{y} - \mathbf{x}_0)\dot{x}^a_0\dot{x}^b_0. \quad (8)$$

Taking the conservation equation for dark matter particles (which, unlike in Li & Zhao (2009, 2010), does not couple to any other matter species, including the scalar field φ), the geodesic equation follows as usual:

$$\ddot{x}_0^a + \Gamma^a_{bc}\dot{x}_0^b\dot{x}_0^c = 0, \tag{9}$$

where the second term on the left-hand side accounts for gravity.

Equations (4), (6), and (9) contain all the physics needed for the following analysis, though certain approximations and simplifications might have to be made in due course to make direct connection to N-body simulations.

We will consider an inverse power-law potential (Ratra & Peebles 1988) for the scalar field

$$V(\varphi) = \frac{\Lambda^4}{(\sqrt{\kappa_*}\varphi)^\alpha}, \tag{10}$$

where α is a dimensionless constant and Λ is a constant with dimensions of mass. This potential has also been adopted in various background or linear perturbation studies of scalar fields (either minimally or non-minimally coupled); the tracking behavior it produces makes it a good dark-energy candidate and for that purpose here we shall choose $\alpha \sim \mathcal{O}(0.1\text{–}1)$ (Caresia et al. 2004; Pettorino & Baccigalupi 2008). Meanwhile, the coupling between the scalar field and the curvature tensor is chosen to be a non-minimal one:

$$f(\varphi) = \gamma\kappa_*\varphi^2, \tag{11}$$

where γ is another dimensionless constant characterizing the strength of the coupling. Note that here again $\kappa_*$is added into $f(\varphi)$ and $V(\varphi)$ to make a dimensionless quantity $\sqrt{\kappa_*}\varphi$. Although the exact value of κ_* is unknown, so is φ and we can solve for $\sqrt{\kappa_*}\varphi$ instead of φ, not caring about the exact individual values of $\sqrt{\kappa_*}$ and φ.

2.2. The Non-relativistic Limits

The N-body simulation only probes the motion of particles at late times, and we are not interested in extreme conditions such as black hole formation and evolution, so we can take the non-relativistic limit of the above equations as a good approximation.

The existence of the scalar field and its coupling to the curvature leads to several possible changes with respect to the ΛCDM paradigm.

1. The scalar field has its own energy–momentum tensor, which could change the source term of the Poisson equation because the scalar field, unlike the cosmological constant, can cluster (though the clustering is often quite weak in scalar field models). Also, unlike in coupled scalar field models, here the $\vec{\nabla}^2\varphi$ term will appear in the Poisson equation.
2. The background cosmic expansion rate is in general modified, and can either slow down or speed up the rate of structure formation.
3. The two gravitational potentials in the conformal Newtonian gauge metric $ds^2 = a^2(1+2\phi)d\tau^2 - a^2(1-2\psi)\delta_{ij}dx^i dx^j$, in which τ and x^i are, respectively, the conformal time and comoving coordinate, are no longer equal to each other (as in general relativity), but are instead related by $\vec{\nabla}^2\varphi$ (see below).

It therefore becomes clear that the following two equations, in their non-relativistic forms, need to be solved in order to obtain the gravitational force on particles:

1. the scalar field equation of motion, which is used to compute *explicitly* the value of the scalar field φ at any given time and position, and
2. the Poisson equation, which is used to determine the gravitational potential and force at any given time and position from the local energy density and pressure, which includes the contribution from the scalar field (obtained from the φ equation of motion).

Note that unlike in the coupled scalar field models, there is no fifth force because there is no direct coupling to the particles. The scalar coupling to the curvature, however, does modify the gravitational potential so that gravity no longer follows Einstein's prescription and so this is a modified gravity theory. Mathematically, the coupled scalar field and scalar–tensor theories are related to each other by a conformal transformation Damour & Esposito-Farese (1992), but often the former has the flexibility that not all matter species are coupled to the scalar field so that local fifth force constraints can be evaded more easily.

We now describe these two equations in turn. For the scalar field equation of motion, we denote by $\bar{\varphi}$ the background value of φ and write $\delta\varphi \equiv \varphi - \bar{\varphi}$. Then using the expressions given in Appendix A we write

$$\begin{aligned} a^2\nabla^a\nabla_a\varphi = {} & \varphi'' + 2\mathcal{H}\varphi' + c^2\vec{\nabla}^2_{\mathbf{x}}\varphi - 2\phi\varphi'' \\ & - (\phi' + 3\psi' + 4\mathcal{H}\phi)\varphi', \end{aligned} \tag{12}$$

in which $' = d/d\tau$ with τ the conformal time, $\vec{\nabla}_{\mathbf{x}}$ is the derivative with respect to the comoving coordinate $\mathbf{x}$, and $\mathcal{H} = a'/a$. Then, with the background part subtracted, Equation (6) can be rewritten as

$$\begin{aligned} & \delta\varphi'' + 2\mathcal{H}\delta\varphi' + c^2\vec{\nabla}^2_{\mathbf{x}}\delta\varphi + [V_{,\varphi}(\varphi) - V_{,\varphi}(\bar{\varphi})]a^2 - 2\phi\bar{\varphi}'' \\ & - (\phi' + 3\psi' + 4\mathcal{H}\phi)\bar{\varphi}' + \frac{1}{2\kappa_*}[Rf_\varphi(\varphi) - \bar{R}f_\varphi(\bar{\varphi})]a^2 = 0, \end{aligned}$$

in which a bar denotes the background value, R is the Ricci scalar, and the subscript $_\varphi$ denotes derivatives with respect to φ. Note that $\vec{\nabla}^2_{\mathbf{x}}$ has the same sign as $\vec{\nabla}^2_{\mathbf{r}}$.

In our N-body simulations, we work in the quasi-static limit, i.e., we assume that the spatial gradients are much greater than the time derivatives, $|\vec{\nabla}_{\mathbf{x}}\delta\varphi| \gg |\frac{\partial\delta\varphi}{\partial\tau}|$. Therefore, the time derivatives in the above equation are dropped and we obtain the simplified version

$$c^2\vec{\partial}^2_{\mathbf{x}}(a\delta\varphi) = a^3[V_\varphi(\varphi) - V_\varphi(\bar{\varphi})] + \frac{1}{2\kappa_*}[Rf_\varphi(\varphi) - \bar{R}f_\varphi(\bar{\varphi})]a^3, \tag{13}$$

in which $\vec{\partial}^2_{\mathbf{x}} = -\vec{\nabla}^2_{\mathbf{x}} = +\left(\partial_x^2 + \partial_y^2 + \partial_z^2\right)$ due to our sign convention $(+,-,-,-)$. Note that here V has the dimension of *mass* density rather than *energy* density.

To complete Equation (13), we still need expressions for R and $\bar{R}$, which are again obtained using the quantities in Appendix A:

$$\begin{aligned} R = {} & -\frac{6}{a^2}\frac{a''}{a}(1-2\phi) \\ & + \frac{1}{a^2}\left[6\psi'' + 6\mathcal{H}(\phi' + 3\psi') - 4\vec{\partial}^2_{\mathbf{x}}\psi + 2\vec{\partial}^2_{\mathbf{x}}\phi\right], \end{aligned} \tag{14}$$

$$\bar{R} = -\frac{6}{a^2}\frac{a''}{a} \tag{15}$$

and so

$$Rf_\varphi - \bar{R}\bar{f}_\varphi \doteq \bar{f}_\varphi \delta R + \bar{R}\delta f_\varphi \doteq -\frac{1}{a^2}\bar{f}_\varphi\left(4\vec{\partial}_{\mathbf{x}}^2\psi - 2\vec{\partial}_{\mathbf{x}}^2\phi\right) - \frac{6}{a^2}\frac{a''}{a}\delta f_\varphi, \quad (16)$$

where we have again dropped time derivatives of ϕ and ψ since they are small compared with the corresponding spatial gradients, and $\delta R \equiv R - \bar{R}$, $\delta f_\varphi \equiv f_\varphi - \bar{f}_\varphi$.

Since only ϕ but not ψ appears in the Poisson equation (shown below), we also want to eliminate ψ in the scalar field equation of motion. This is easy in general relativity, because there we have the simple relation $\phi = \psi$, which unfortunately no longer holds in scalar–tensor theories. However, we could use the i–j components of the Einstein equation $G^i{}_j = \kappa_* T^i{}_j$ $(i \neq j)$ to get a new relation between ϕ and ψ. Noting that our N-body simulations probe the very late time evolution (when radiation is negligible) when the only significant source for $T^i{}_j$ $(i \neq j)$ is the scalar field, and

$$\nabla^i \nabla_j f = -\frac{1}{a^2}\partial_i \partial_j f \quad (i \neq j), \quad (17)$$

where $\partial_i \equiv \partial/\partial x^i$, we could write the i–j component of the Einstein equation as

$$\partial_i \partial_j(\phi - \psi) = -\frac{c^2}{1+f}\partial_i \partial_j f,$$

which gives approximately (i.e., neglecting second-order terms such as $\partial_i f \partial_j f$ compared to first-order terms such as $\partial_i \partial_j f$) by integrating once

$$\partial_i(\phi - \psi) = -\frac{c^2}{1+f}\partial_i f$$

and so

$$4\vec{\partial}_{\mathbf{x}}^2\psi - 2\vec{\partial}_{\mathbf{x}}^2\phi \doteq 2\vec{\partial}_{\mathbf{x}}^2\phi + \frac{4}{1+f}\vec{\partial}_{\mathbf{x}}^2 f \doteq 2\vec{\partial}_{\mathbf{x}}^2\phi + \frac{4\bar{f}_\varphi}{1+\bar{f}}c^2\vec{\partial}_{\mathbf{x}}^2\delta\varphi. \quad (18)$$

It is important to note that in the second line of Equation (18) we have implicitly linearized the equation; this is valid only if $f(\varphi)$ is not strongly nonlinear and $|\delta\varphi/\varphi| \ll 1$. It turns out that the model considered in this work satisfies these criteria ($f(\varphi) \propto \varphi^2$). If either $V(\varphi)$ or $f(\varphi)$ is highly nonlinear, then we might have $|\delta\varphi| \sim \varphi$; in that case, we should not approximate f to $\bar{f}$ even in the coefficients of the perturbation variables such as $\vec{\partial}_{\mathbf{x}}^2\delta\varphi$ here, or write $\vec{\partial}_{\mathbf{x}}^2 f = \bar{f}_\varphi \vec{\partial}_{\mathbf{x}}^2\delta\varphi$. The reason for the latter stricture is as follows: if $f(\varphi)$ is highly nonlinear, then f might change significantly even if φ fluctuates only slightly, implying that for the linearization to apply on our spatial grid we need very small grid sizes, which are impossible; moreover, it becomes complicated to decide which solution we should linearize around, as the values of f in the area that we look at might be very different from the background value $\bar{f}$. The strategy for this situation is simple: instead of writing $\vec{\partial}_{\mathbf{x}}^2 f = \bar{f}_\varphi \vec{\partial}_{\mathbf{x}}^2\delta\varphi$, we difference $f(\varphi)$ directly, because we know the value of $f(\varphi)$ in every grid cell. This will ensure no linearization error. In what follows, however, we use Equation (18), which causes negligible linearization error but greatly simplifies the equations. We also write $f \doteq \bar{f}$ in the coefficients of perturbation quantities such as $\vec{\partial}_{\mathbf{x}}^2\delta\varphi$ and $\vec{\partial}_{\mathbf{x}}^2\Phi$ (where we have defined $\Phi \equiv a\phi$ for later convenience).

Substituting Equations (16) and (18) into Equation (13) and rearranging, we complete the derivation of the scalar field equation of motion in the weak field limit, ending up with

$$\left[1 + \frac{2\bar{f}_\varphi^2}{\kappa_*(1+\bar{f})}\right]c^2\vec{\partial}_{\mathbf{x}}^2(a\delta\varphi) = a^3[V_\varphi(\varphi) - V_\varphi(\bar{\varphi})] - \frac{\bar{f}_\varphi}{2\kappa_*}\vec{\partial}_{\mathbf{x}}^2\Phi - \frac{3}{\kappa_*}\frac{a''}{a}a\delta f_\varphi \quad (19)$$

for our general Lagrangian Equation (1) and

$$\left[1 + \frac{8\gamma^2\kappa_*\bar{\varphi}^2}{1+\gamma\kappa_*\bar{\varphi}^2}\right]c^2\vec{\partial}_{\mathbf{x}}^2(a\sqrt{\kappa_*}\delta\varphi) = -\gamma\sqrt{\kappa_*}\bar{\varphi}\vec{\partial}_{\mathbf{x}}^2\Phi - 6\gamma(\mathcal{H}' + \mathcal{H}^2)(a\sqrt{\kappa_*}\delta\varphi) - \alpha\kappa_*\Lambda^4 a^3\left[\frac{1}{(\sqrt{\kappa_*}\varphi)^{1+\alpha}} - \frac{1}{(\sqrt{\kappa_*}\bar{\varphi})^{1+\alpha}}\right] \quad (20)$$

for the model specified by Equations (10) and (11).

Next consider the Poisson equation, which is obtained from the Einstein equation in the weak-field and slow-motion limits. Here we use the 0–0 component of the Ricci curvature tensor, which is given as

$$R^0{}_0 = -3\left(\frac{a''}{a} - \mathcal{H}^2\right)(1 - 2\phi) + 3\psi'' + 3\mathcal{H}(\psi' + \phi') + \vec{\partial}_{\mathbf{x}}^2\phi \quad (21)$$

using the expressions in Appendix A. According to the Einstein equations,

$$R^0{}_0 = \frac{\kappa_*}{2}(\rho_{\rm TOT} + 3p_{\rm TOT})a^2, \quad (22)$$

where $\rho_{\rm TOT}$ and $p_{\rm TOT}$ are the total energy density and pressure, respectively. Using these two equations and subtracting the background part (which is just the Raychaudhuri equation), it is straightforward to find that

$$\vec{\partial}_{\mathbf{x}}^2\Phi = \frac{\kappa_* a^3}{2}\left[(\rho_{\rm TOT} + 3p_{\rm TOT}) - (\bar{\rho}_{\rm TOT} + 3\bar{p}_{\rm TOT})\right], \quad (23)$$

in which we have dropped terms involving time derivatives of ψ, ϕ, and $\mathcal{H}^2\phi$, because they are much smaller than $\vec{\partial}_{\mathbf{x}}^2\phi$ in the quasi-static limit. Using the energy–momentum tensor expressed in Equation (4), the above equation can be rewritten as

$$\vec{\partial}_{\mathbf{x}}^2\Phi \doteq \frac{\kappa_* a^3}{2}\bar{\rho}_m\left(\frac{\delta}{1+f} - \frac{1}{1+\bar{f}}\right) - \frac{\bar{f}_\varphi}{2(1+\bar{f})}c^2\vec{\partial}_{\mathbf{x}}^2(a\delta\varphi) - \kappa_* a^3\left[\frac{V(\varphi)}{1+f} - \frac{V(\bar{\varphi})}{1+\bar{f}}\right] + a\left(\frac{1}{1+f} - \frac{1}{1+\bar{f}}\right)\left(\kappa_*\bar{\varphi}'^2 + \frac{3}{2}f''\right) \quad (24)$$

for the general Lagrangian equation (Equation (1)) and

$$\vec{\partial}_{\mathbf{x}}^2 = \frac{3}{2}\left(1+\gamma\kappa_*\bar{\varphi}_0^2\right)\Omega_m H_0^2\left[\frac{\delta}{1+\gamma\kappa_*\varphi^2}-\frac{1}{1+\gamma\kappa_*\bar{\varphi}^2}\right] - \frac{\gamma\sqrt{\kappa_*}\bar{\varphi}}{1+\kappa_*\bar{\varphi}^2}c^2\vec{\partial}_{\mathbf{x}}^2(a\sqrt{\kappa_*}\delta\varphi) - \left[\frac{\kappa_*\Lambda^4a^3}{(1+\gamma\kappa_*\varphi^2)(\sqrt{\kappa_*}\varphi)^\alpha}-\frac{\kappa_*\Lambda^4a^3}{(1+\gamma\kappa_*\bar{\varphi}^2)(\sqrt{\kappa_*}\bar{\varphi})^\alpha}\right] + [(1+3\gamma)\kappa_*\bar{\varphi}'^2+3\gamma\kappa_*\bar{\varphi}\bar{\varphi}'']a \times\left[\frac{1}{1+\gamma\kappa_*\varphi^2}-\frac{1}{1+\gamma\kappa_*}\bar{\varphi}^2\right] \quad (25)$$

for the model specified by Equations (10) and (11). In these equations, $\bar{\rho}_m$ is the background density for matter, $\delta \equiv \rho_m/\bar{\rho}_m$, and we have used the definition of Ω_m given in Appendix C. We have also neglected the contribution from $\delta\varphi$ to the total density and pressure, because in the quasi-static limit we have $|\delta\varphi''| \ll |\vec{\partial}_{\mathbf{x}}^2\delta\varphi|$and $\delta\varphi'^2 \lesssim |\bar{\varphi}'\delta\varphi'| \lesssim |\mathcal{H}\delta\varphi'| \ll \vec{\partial}_{\mathbf{x}}^2\delta\varphi|$ (which is confirmed by the N-body simulation results[4]).

Finally, the equation of motion of the dark matter particles is the same as in general relativity:

$$\ddot{\mathbf{x}} + 2\frac{\dot{a}}{a}\dot{\mathbf{x}} = -\frac{1}{a^3}\vec{\nabla}_{\mathbf{x}}\Phi, \quad (26)$$

in which Φ is determined by the modified Poisson equation (Equation (25)). The canonical momentum conjugate to $\mathbf{x}$ is $\mathbf{p} = a^2\dot{\mathbf{x}}$, so from the equation above we have

$$\frac{d\mathbf{x}}{dt} = \frac{\mathbf{p}}{a^2}, \quad (27)$$

$$\frac{d\mathbf{p}}{dt} = -\frac{1}{a}\vec{\nabla}_{\mathbf{x}}\Phi. \quad (28)$$

Equations (20), (25), (27), and (28) will be used in the code to evaluate the forces on the dark matter particles and evolve their positions and momenta in time. But before applying them to the code we still need to switch to code units (see Section 2.3), further simplify them, and create the discrete version (see Appendix B).

2.3. Code Units

In our numerical simulation, we use a modified version of MLAPM (Knebe et al. 2001), and we will have to change or add our Equations (20), (25), (27), and (28) to it. The first step is to convert the quantities to the code units of MLAPM. Here, we briefly summarize the main results.

The (modified) MLAPM code uses the following internal units (where a subscript $_c$ stands for "code"):

$$\mathbf{x}_c = \mathbf{x}/B,$$

$$\mathbf{p}_c = \mathbf{p}/(H_0B)$$

$$t_c = tH_0$$

$$\Phi_c = \Phi/(H_0B)^2$$

$$\rho_c = \rho/\bar{\rho},$$

$$\delta\varphi_c = u = ac^2\sqrt{\kappa}\delta\varphi/(H_0B)^2, \quad (29)$$

where B denotes the comoving size of the simulation box, H_0 is the present Hubble constant, and ρ is the matter density. In the last line, the quantity u is the scalar field *perturbation* $\delta\varphi$ expressed in terms of code units and is new to the MLAPM code.

In terms of u, as well as the (dimensionless) background value of the scalar field, $\sqrt{\kappa}\bar{\varphi}$, some relevant quantities are expressed in full as

$$V(\varphi) = \frac{\Lambda^4}{\left(\sqrt{\kappa}\bar{\varphi}+\frac{B^2H_0^2}{ac^2}u\right)^\alpha},$$

$$f(\varphi) = 1+\gamma\left(\sqrt{\kappa}\bar{\varphi}+\frac{B^2H_0^2}{ac^2}u\right)^2,$$

$$V_\varphi(\varphi) = -\alpha\frac{\sqrt{\kappa}\Lambda^4}{\left(\sqrt{\kappa}\bar{\varphi}+\frac{B^2H_0^2}{ac^2}u\right)^{1+\alpha}},$$

$$f_\varphi(\varphi) = 2\gamma\sqrt{\kappa}\left(\sqrt{\kappa}\bar{\varphi}+\frac{B^2H_0^2}{ac^2}u\right), \quad (30)$$

and the background counterparts of these quantities can be obtained simply by setting $u = 0$ (recall that u represents the perturbed part of the scalar field) in the above equations.

We also define

$$\lambda \equiv \frac{\kappa\Lambda^4}{3H_0^2}, \quad (31)$$

which will be used frequently below.

Making discrete versions of the above equations for N-body simulations is then straightforward, and we refer the interested readers to Appendix B for the whole treatment, with which we can now proceed to conduct N-body simulations.

3. SIMULATION DETAILS

3.1. The N-Body Code

The MLAPM code we have modified for our simulations is a self-adaptive multi-level particle-mesh code. It has two sets of grids (or meshes). The first set is a series of regular grids covering the cubic simulation box with $N = 2, 4, 8, 16, \ldots$ cells on one side, the finest of which is called the domain grid. This set of grids can be used to compute the gravitational potential using either fast Fourier transform (in this case only the domain grid is used) or multigrid relaxation methods (Press et al. 1992). The second set is refined grids, which are created on-the-fly when the particle density in some region exceeds a given threshold. The refinements make sure that higher spatial resolution is used in high-density regions, and as such they can have arbitrary shapes; the gravitational potential is solved on the refined grids using single-grid relaxation (Press et al. 1992). For more detailed descriptions see Li & Zhao (2010) and Li & Barrow (2011).

[4] According to Equation (20), we have $\vec{\partial}_{\mathbf{x}}^2(a\sqrt{\kappa_*}\delta\varphi) \sim \mathcal{O}(\vec{\partial}_{\mathbf{x}}^2\Phi)$, implying that $a\sqrt{\kappa_*}\delta\varphi \sim \mathcal{O}(\Phi)$, so neglecting time derivatives of $\delta\varphi$ is just like dropping time derivatives of ψ and ϕ, which we have already done to obtain the modified Poisson equation.

Some of our main modifications to the MLAPM code for the coupled scalar field model are as follows.

1. We have added a solver for the scalar field, based on Equation (B7). It uses a nonlinear Gauss–Seidel scheme (Press et al. 1992) for the relaxation iteration and the same criterion for convergence as the default Poisson solver. But it adopts a V-cycle (Press et al. 1992) instead of the self-adaptive scheme in arranging the Gauss–Seidel iterations. Note that the scalar field and the Poisson equation are solved on the same grids in our simulations.
2. The value of u solved in this way is then used to calculate the total matter density, which completes the calculation of the source term for the Poisson equation.
3. The gravitational potential Φ is solved using fast Fourier transform on the domain grid and relaxation on the refinements so that we know its value Φ_{ijk} on any grid cell indexed by i, j, k, respectively, in the x, y, z directions. It is then used to compute the (modified) gravitational force by finite difference (which is the discrete version of differentiation). Finally, the force computed thereby is used to displace and kick the particles.

There are a lot of additions and modifications to ensure a smooth interface and the newly added data structures. For the output, as there are multilevel grids, all of which host particles, the composite grid is inhomogeneous and we therefore choose to output the positions and momenta of the particles, plus the gravity and values of Φ and u at the positions of these particles. We also output the potential and scalar field values on the 128^3 domain grid.

3.2. Physical and Simulation Parameters

The physical parameters we use in the simulations are as follows: the present-day dark-energy fractional energy density $\Omega_{\rm DE} = 0.743$ and $\Omega_m = \Omega_{\rm CDM} + \Omega_{\rm B} = 0.257$, $H_0 = 71.9\ {\rm km\,s^{-1}\,Mpc^{-1}}$, $n_s = 0.963$, $\sigma_8 = 0.769$.[5] Our simulation box has a size of $64\,h^{-1}$ Mpc, where $h = H_0/(100\,{\rm km\,s^{-1}\,Mpc^{-1}})$. We simulate four models, with parameters $(\alpha, \gamma) = (0.1, -0.2)$, $(0.1, 0.2)$, $(0.5, -0.2)$, and $(0.5, 0.2)$, respectively. In all those simulations, the mass resolution is $1.114 \times 10^9\,h^{-1}M_\odot$, the particle number is 256^3, the domain grid is a $128 \times 128 \times 128$ cubic, and the finest refined grids have 16,384 cells on each side, corresponding to a force resolution of about $12\,h^{-1}$ kpc. The force resolution determines the smallest scale on which the numerical results are reliable.

We also run a ΛCDM simulation with the same physical parameters and initial condition (see below).

3.3. Background and Linear Perturbation Evolution

Since the coupling between the scalar field and the curvature produces a time-varying effective gravitational constant, and the scalar field contributes to the total energy–momentum tensor, we expect that cosmology in the extended quintessence models is generally different from ΛCDM at the background and linear perturbation levels. A good understanding of this will be helpful in our analysis of the results from N-body simulations, and this is the subject of this subsection.

Our algorithm and formulae for the background cosmology are detailed in Appendix C, and are implemented in MAPLE. We output the relevant quantities in a predefined time grid, which could be used (via interpolation) in the linear perturbation and N-body computations.

Figure 1 shows the time evolution of some background quantities of interest. For ease of comparison we have chosen Ω_m and Ω_r to be the same in all models including the ΛCDM one (for definitions of Ω_m and Ω_r, see Appendix C), and as a result, in the upper left panel the curves for different models converge at common right-hand ends. We see increasing α results in an earlier and slower growth of $\Omega_{\rm DE}$ ($\Omega_{\rm DE} = 1 - \Omega_m - \Omega_r$). This indicates a larger dark-energy equation of state parameter, w, which is confirmed by the upper right panel. Physically, this is because, the larger α is, the steeper the potential becomes and thus the faster the scalar field rolls. Note that w is also larger for positive γ, with α being the same. This is because in Equation (6) the Ricci scalar $R < 0$ and for positive γ the term $\frac{R}{2\kappa_*} f_\varphi$ has the same sign as V_φ, thus helping the scalar field to roll faster. Because of the large magnitude and almost-constant predicted w, the model $(\alpha, \gamma) = (0.5, 0.2)$ is already excluded by cosmological data, but here we keep it for purely theoretical interest (i.e., to see how changing α or γ changes the nonlinear structure formation).

We are also interested in how the expansion rate in an extended quintessence model differs from that in ΛCDM, and the results for our models are shown in the lower left panel of Figure 1, which plots the $H/H_{\Lambda\rm CDM}$ as a function of a. The rather odd behavior of the models at low redshift is because of the complicated evolution of the scalar field (and the fact that we have chosen H_0 to be the same for all models, again for ease of comparison), while the high-redshift behavior could be seen directly from Equation (C4). In Equation (C4), the energy density of the scalar field can be dropped at high z, and so we have

$$\left(\frac{\mathcal{H}}{\mathcal{H}_0}\right)^2 \approx \frac{1+f_0}{1+f}\Omega_m a^{-1}, \tag{32}$$

where we have also neglected the radiation for simplicity (which is valid after the matter-radiation equality). This shows that in extended quintessence models the gravitational constant relevant for the background cosmology is rescaled by $(1 + f_0)/(1 + f)$. Because $f_0 = f(\varphi_0)$, where φ_0 is the present-day value of φ, and φ is monotonically increasing in time, for our choice of $f(\varphi)$ (cf. Equation (11)) we have $(1 + f_0)/(1 + f) > 1$ for $\gamma > 0$ and $(1 + f_0)/(1 + f) < 1$ for $\gamma < 0$; thus, models with $\gamma > 0$ have $H/H_{\Lambda\rm CDM} > 1$.

It turns out that the gravitational constant relevant for the growth of matter density perturbations is also different from the one governing the background cosmology. If we denote the matter density perturbation by δ_m, then it can be shown, using the linear perturbation equations, that on small scales the evolution equation for δ_m reduces to

$$\delta_m'' + \mathcal{H}\delta_m' = G_{\rm N}\frac{3\mathcal{H}_0^2}{2}\Omega_m\delta_m a^2, \tag{33}$$

[5] The σ_8 is used only to generate initial conditions. To be more explicit, in the ideal case the initial condition for the scalar–tensor models is generated as follows: (1) choose a ΛCDM model for which $\sigma_8 = 0.769$, (2) evolve its linear power spectrum backward up to $z \sim 10^6$, (3) evolve this initial power spectrum forward using the scalar–tensor model up to $z \sim 49$, and (4) generate the initial condition for scalar–tensor N-body simulations using this new power spectrum and Zel'dovich approximation (Li & Barrow 2011). As a result, the σ_8 is only used to make sure that all our simulations (scalar–tensor and ΛCDM) have the same initial condition at $z \sim 10^6$ (when the influence of the scalar field is negligible), and they do not necessarily have the same σ_8 at $z \sim 49$ or $z = 0$.

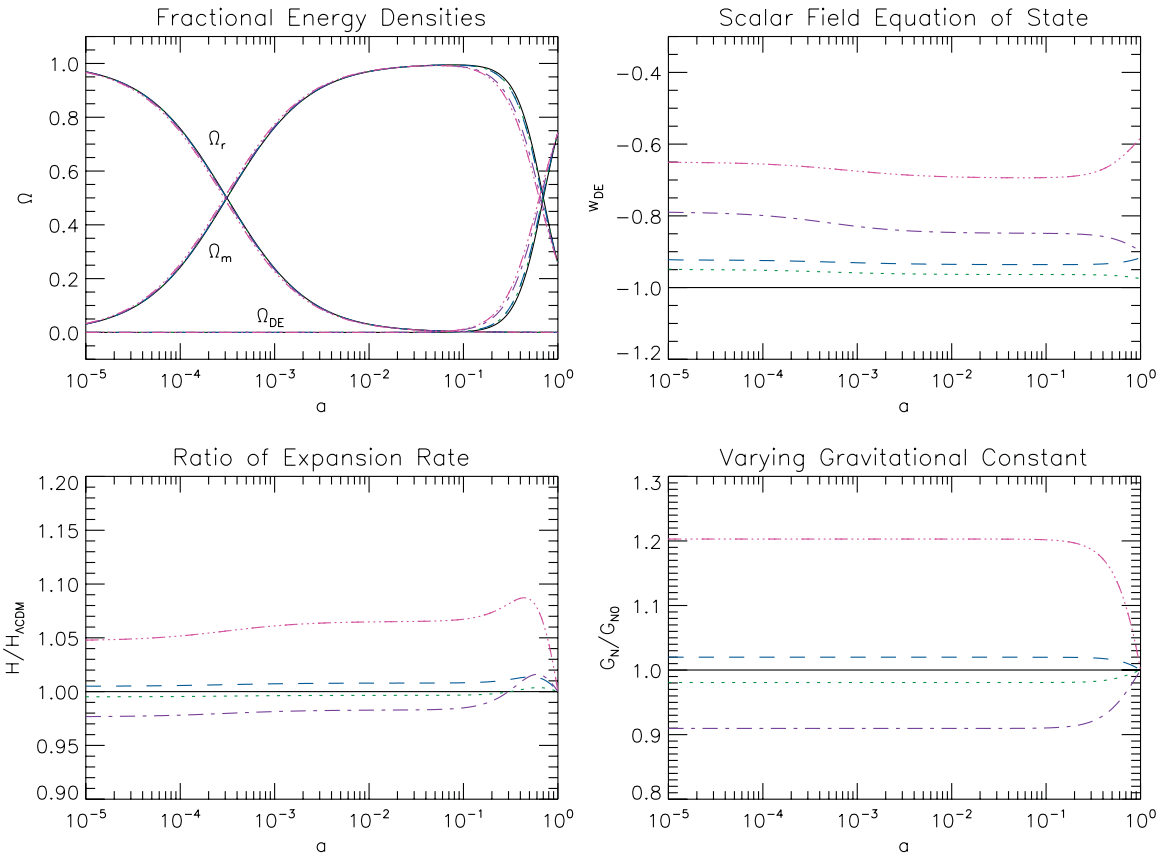

Figure 1. Background evolution in the extended quintessence models. Upper left panel: the fractional energy densities for matter (Ω_m), radiation (Ω_r), and the scalar field dark energy ($\Omega_{\rm DE}$), as indicated beside the curves, as functions of the scale factor a ($a_0 = 1$ today). Upper right panel: the scalar field equation of state $w = p_{\rm DE}/\rho_{\rm DE}$ as a function of a. Lower left panel: the ratio between the Hubble expansion rates of the extended quintessence model and ΛCDM as a function of a. Lower right panel: the a-evolution of the effective gravitational constant that governs the growth of matter density perturbations ($G_{\rm N0}$ is its value today). In all panels, the black solid, green dot, blue dashed, purple dot-dashed, pink dot-dot-dot-dashed curves represent, respectively, the results for ΛCDM and extended quintessence models with $(\alpha, \gamma) = (0.1, -0.2)$, $(0.1, 0.2)$, $(0.5, -0.2)$, $(0.5, 0.2)$.

(A color version of this figure is available in the online journal.)

in which $' \equiv d/d\tau$ and τ is the conformal time (see Appendix C), and we have defined

$$G_{\rm N} \equiv \frac{1+f_0}{1+f}\frac{2+2f+4\left(\frac{df}{d\sqrt{\kappa_*}\varphi}\right)^2}{2+2f+3\left(\frac{df}{d\sqrt{\kappa_*}\varphi}\right)^2}. \quad (34)$$

Note that this quantity could also be directly read off from the modified Poisson equation (Equation (B3)).

In the lower right panel of Figure 1, we display the evolution for $G_{\rm N}$ in the models considered. Again, $G_{\rm N}$ is larger at earlier times for positive γ and smaller for negative γ, because of our specific choice of $f(\varphi)$ in Equation (11), and the fact that φ is always increasing in time. From our results we can estimate how fast $G_{\rm N}$ is varying today, and we find that $|\dot{G}_{\rm N}/G_{\rm N}| \sim 1.68 \times 10^{-12}$, 2.71×10^{-12}, 6.86×10^{-12}, and $2.27 \times 10^{-11}\,{\rm yr}^{-1}$, respectively, for the models with $(\alpha, \gamma) = (0.1, -0.2)$, $(0.1, 0.2)$, $(0.5, -0.2)$, and $(0.5, 0.2)$. The experimental constraints on $|\dot{G}_{\rm N}/G_{\rm N}|$ still suffer from uncertainties (Uzan 2010), and a conservative estimate is $|\dot{G}_{\rm N}/G_{\rm N}| \leqslant 1 \times 10^{-11}$. This means that our first three models are compatible with the constraints while the last one violates them slightly. Once again, we continue studying it for purely theoretical interests.

It is well known that a higher rate of background expansion means that structures have less time to form, and a larger $G_{\rm N}$ speeds up the structure formation. These two effects therefore cancel each other to some extent, which results in a weaker net effect of an extended quintessence field on the large-scale structure formation. This is confirmed by our linear perturbation computation depicted in Figure 2. In the right-hand panels of this figure, we have plotted the matter power spectra for different models at two different redshifts (0 and 49). It is interesting to note that on small scales the matter power is closer to that of ΛCDM, despite the significant differences in background expansion rate and $G_{\rm N}$ (cf. Figure 1). Because of this, we choose ΛCDM initial condition for our N-body simulations for all our models, saving the effort of generating separate initial conditions for different models.

The left-hand panels of Figure 2 display the cosmic microwave background (CMB) power spectra for the models we consider. Again the difference from ΛCDM is fairly small, and there is only a small shift of the CMB peaks even though the background expansion rate changes quite a bit. The latter is because peak positions are determined by the ratio of the sound horizon size at decoupling and the angular distance to the decoupling, and in our model both of these decrease/increase as the universe expands faster/more slowly, their ratio does not change much.

To briefly summarize, the study of background cosmology and linear perturbation shows that a modified background expansion rate and a rescaled gravitational constant, the two most important factors affecting structure formation in extended quintessence models are opposite effects. It is then of

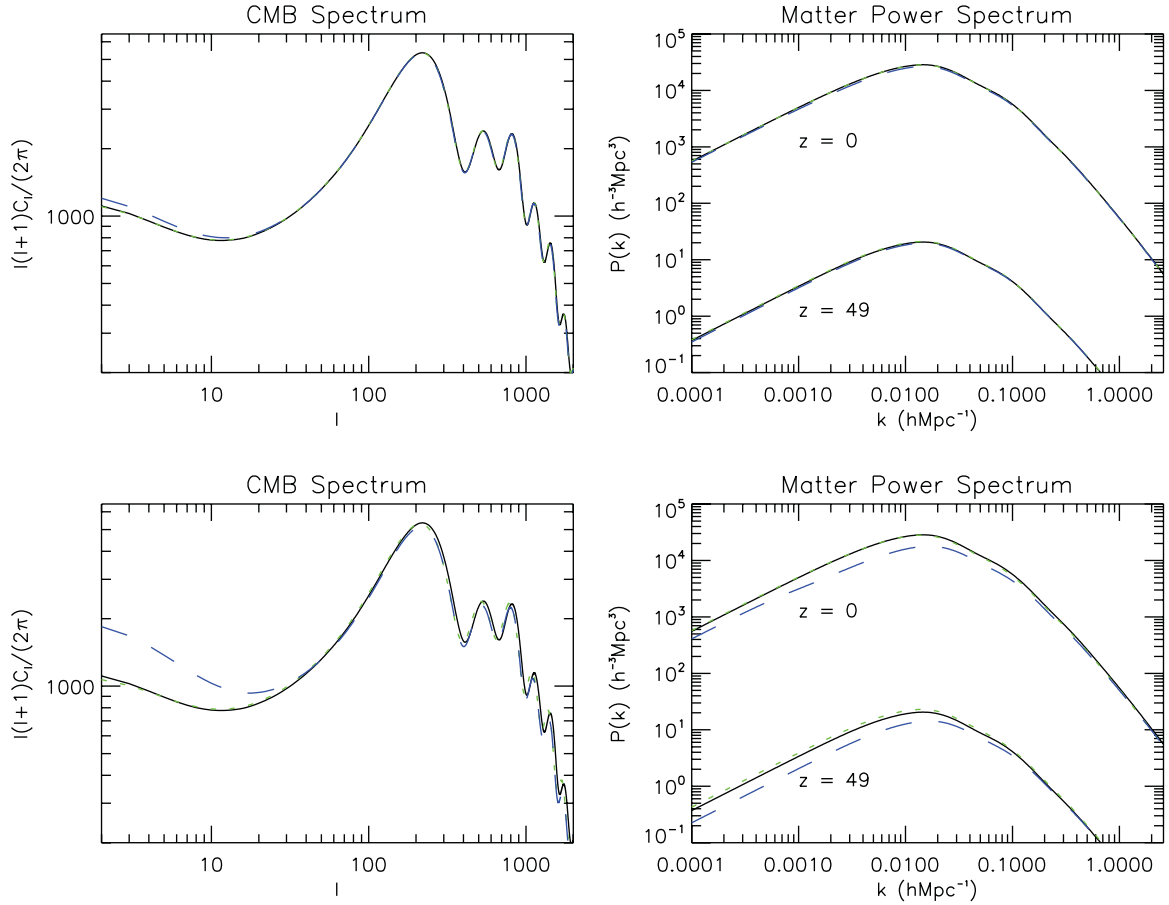

Figure 2. CMB (left panels) and matter power spectra (right panels) for the extended quintessence models compared with those of the ΛCDM. The upper panels are for the models with $\alpha = 0.1$ while the lower panels are for those with $\alpha = 0.5$. The black solid, green dotted, and blue dashed curves represent, respectively, the curves for ΛCDM and extended quintessence with $\gamma = -0.2$ and $\gamma = 0.2$. For the matter power spectra, we plot the results for two different output redshifts, $z = 0$ and 49, as indicated below the curves.

(A color version of this figure is available in the online journal.)

interest to see how these two effects compete in the nonlinear regime.

4. *N*-BODY SIMULATION RESULTS

This section lists the results of extended quintessence *N*-body simulations. We start with a few preliminary results, which both give some basic idea about the extended quintessence effects and serve as a cross check of our codes. Then we discuss the key observables for the nonlinear structure formation such as the matter power spectrum, mass function, and halo properties. We also comment on the halo profile of the scalar field and the spatial variation of gravitational constant.

4.1. Preliminary Results

As mentioned above, in both the linear and *N*-body codes we compute background quantities via an interpolation of some pre-computed table. Because background cosmology is important in determining the structure formation, it is important to check its accuracy. For this we have recorded the ages of the universe today for different models as computed by these two codes, and the results are compatible with each other very well indeed.

Because one of the advantages of our *N*-body code is that it solves the scalar field perturbation explicitly, it is important to check that the solution is within our expectations. From Equations (B1) and (B2) it could be seen clearly that if the contribution to the local density and pressure from the scalar field is negligible compared with that from matter, then the modified Poisson equation and scalar field equation of motion end up with the same source term (up to a $\bar{\varphi}$-dependent coefficient). In this situation, we expect

$$u = -\frac{2\gamma\sqrt{\kappa_*}\bar{\varphi}}{1+\frac{8\gamma^2\kappa_*\bar{\varphi}^2}{1+\gamma\kappa_*\bar{\varphi}^2}}\Phi_c, \tag{35}$$

which means that u is simply proportional to Φ_c with a time-dependent coefficient. In Figure 3, we have checked this relation explicitly: we select a thin slice of the simulation box, fetch the values for u and Φ_c at the positions of the particles (about 10,000 in total) therein, and display them as scatter plots. The solid curve is the approximation of Equation (35), while the green dots are simulation results; we can see that they agree very well with each other, showing that the above approximation is a good one. Note that the scalar field perturbation $a\sqrt{\kappa_*}\delta\varphi$ is generally less than 10^{-6}, compared with the background value $\sqrt{\kappa_*}\bar{\varphi} \sim \mathcal{O}(0.1\text{–}1)$. This confirms that it is consistent to neglect the perturbation in scalar field density/pressure, drop terms such as $\delta\varphi$ and $\ddot{\delta\varphi}$, and replace φ by $\bar{\varphi}$ in coefficients of perturbation quantities such as $\vec{\partial}^2_{\mathbf{x}}\left(a\sqrt{\kappa_*}\delta\varphi\right)$and $\vec{\partial}^2_{\mathbf{x}}\Phi$. It also serves as a check of the numerical code.

As a final consistency check, let us consider the total gravitational force on particles. In extended quintessence models,

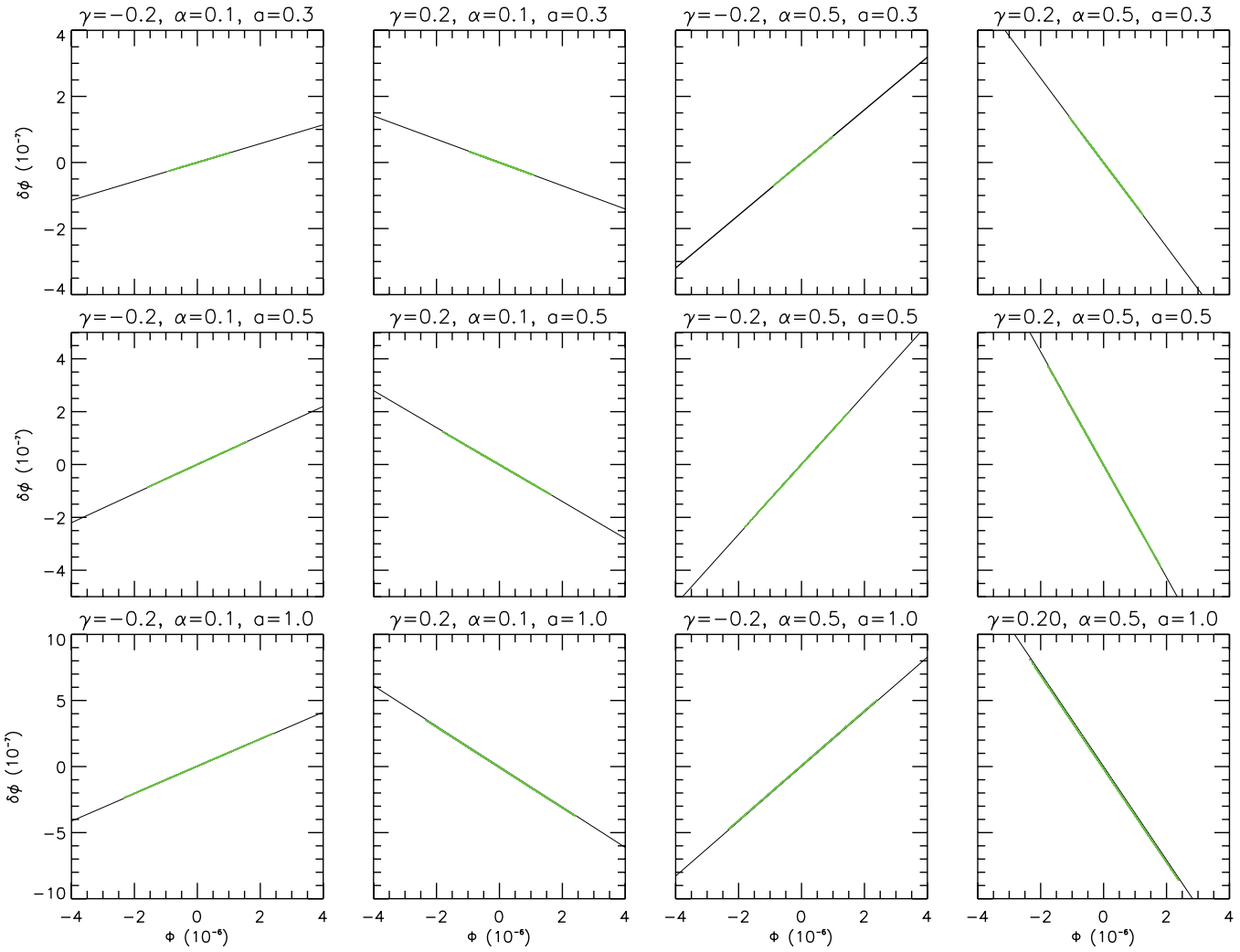

Figure 3. Relation between the magnitudes of the scalar field perturbation $a\sqrt{\kappa_* \delta\varphi}$ (in unit of 10^{-7}) and gravitational potential Φ (in unit of 10^{-6}) for the four extended quintessence models (the four columns) at three different output times $a = 0.3, 0.5, 1.0$ (the three rows) as indicated above the frames. The black solid line in each panel represents the analytical approximation (Equation (35); see the text) and the ∼10,000 green dots represent the results from a thin slice of our simulation boxes.

(A color version of this figure is available in the online journal.)

this is given by Equation (B2), and when the perturbation in the scalar field density/pressure is negligible (which is the case as shown above) we get

$$\nabla^2 \Phi_c \approx \frac{3}{2} G_{\rm N} \Omega_m H_0^2 \left(\rho_c - 1\right), \tag{36}$$

in which $G_{\rm N}$ is given in Equation (34). On the other hand, if we consider (naïvely) that gravity is described by general relativity, then we should neglect the $G_{\rm N}$ on the right-hand side. Manipulating Equations (B1) and (B2) we obtain

$$\frac{1+\gamma\kappa_*\bar{\varphi}_0^2}{1+\gamma\kappa_*\bar{\varphi}^2}\nabla^2\left(\Phi_c + \frac{\gamma\sqrt{\kappa_*}\bar{\varphi}}{1+\gamma\kappa_*\bar{\varphi}^2}u\right) \approx \frac{3}{2}\Omega_m H_0^2\left(\rho_c - 1\right).$$

Thus, $\frac{1+\gamma\kappa_*\bar{\varphi}_0^2}{1+\gamma\kappa_*\bar{\varphi}^2}(\Phi_c + \frac{\gamma\sqrt{\kappa_*}\bar{\varphi}}{1+\gamma\kappa_*\bar{\varphi}^2}u)$ acts as the potential for naïve gravity (i.e., general relativity) and by differencing it we could obtain the naïve gravitational force. In Figure 4, we show the scatter plot of the naïve gravity versus full gravity for the same particles as in Figure 3 (green dots) as well as their approximate ratio $G_{\rm N}$ (solid line). Again, the agreement is remarkably good.

4.2. Nonlinear Matter Power Spectrum

As we have seen above, the linear matter power spectrum for the extended quintessence model really does not show much useful information on small scales, and so we need to investigate whether nonlinear effects could change this situation and therefore potentially place more meaningful constraints.

Figure 5 provides a positive answer to this question. Here, we have plotted the fractional difference of the extended quintessential nonlinear matter power spectrum from that for ΛCDM (remember that we use the same initial condition for all simulations). We can see that for the models with $\alpha = 0.1$ the differences are small even in the nonlinear regime, indicating that the scalar field really does not affect the matter distribution significantly if the potential is flat. However, for the $\alpha = 0.5$ cases in which the coupling strength γ remains the same, the difference could be as large as 30%–50%, guaranteeing an observable signature.

Furthermore, for negative γ (the purple curve) the extended quintessential power spectrum exceeds the ΛCDM one on small scales, whereas for the positive γ case (the pink curve) it

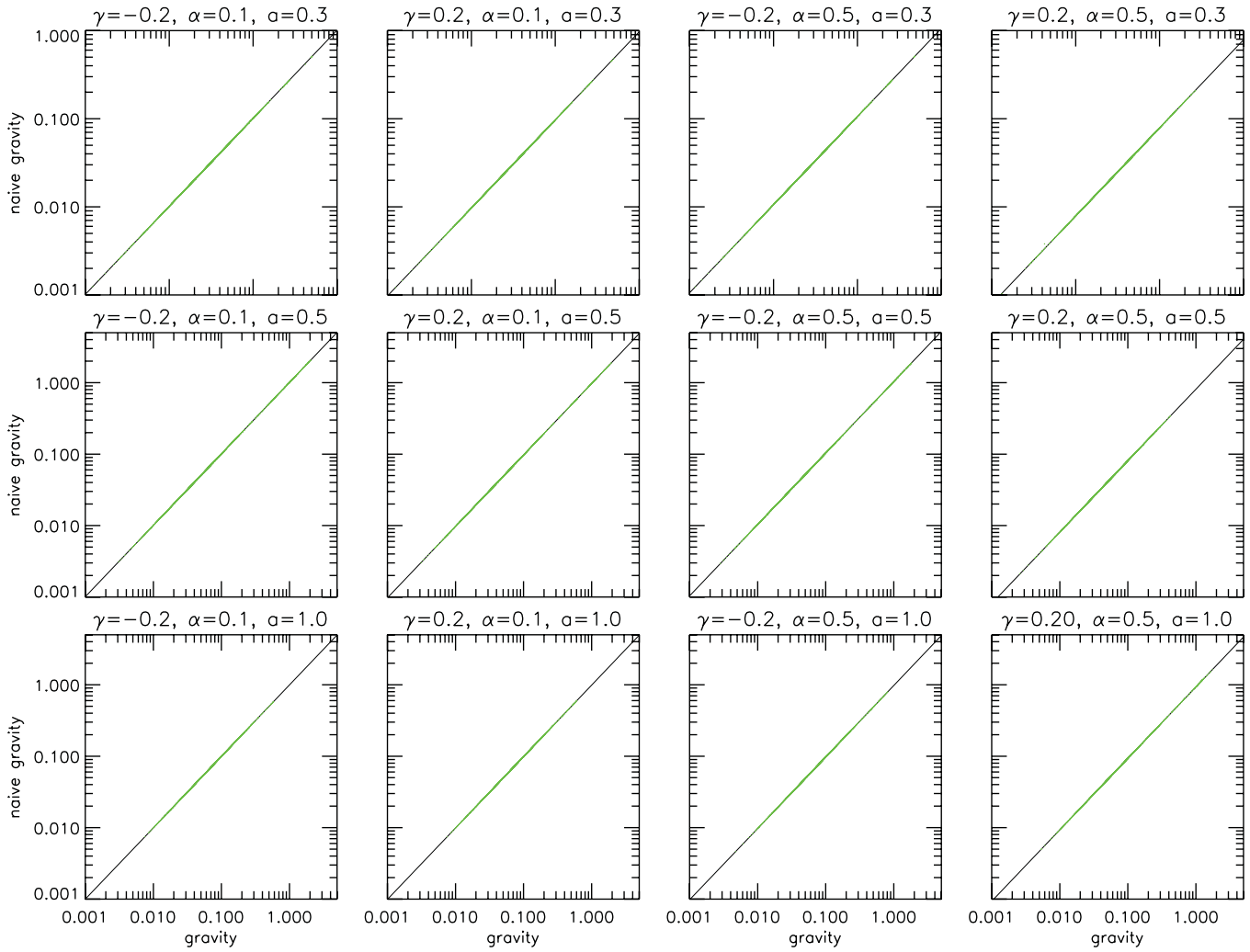

Figure 4. Relation between the magnitudes of the naïve gravity (see the text) and full gravity for the four extended quintessence models (the four columns) at three different output times $a = 0.3, 0.5, 1.0$ (the three rows) as indicated above the frames. The black solid line in each panel represents the analytical approximation (Equation (34); see the text) and the ∼10,000 green dots represent the results from the simulations.

(A color version of this figure is available in the online journal.)

is just the opposite. As shown before, when $\gamma < 0$, both the background expansion rate and the effective gravitational constant governing the structure formation decrease, boosting and weakening the collapse of matter, respectively. In our $\alpha = 0.5$ cases, the first effect has clearly taken over on small scales.

For comparison, we also plot the linear perturbation result of $\Delta P / P_{\Lambda\mathrm{CDM}}$ in Figure 5, which shows how much of the deviation from ΛCDM is due to nonlinear evolution. On large scales, the linear and nonlinear results agree reasonably well, and the up-to-few-percent difference at $k = 0.1\,h\,\mathrm{Mpc}^{-1}$ is because we use ΛCDM initial conditions for all the N-body simulations.

A clearer way to quantify the effect of the scalar field on the nonlinear structure formation is to plot the nonlinear matter power spectra at common linear growth factors, as is done by Jennings et al. (2010). In this way, one can isolate the differences in $P(k)$, which are beyond the differences in the linear growth factor, and are therefore very informative (see Angulo & White 2010 for a development of this idea to rescale one simulation to get another for a different cosmology). Unfortunately, our output frequency is too low to make such an analysis, and we shall leave this for future works.

4.3. Mass Function

A second important observable is the mass function. This gives the number density of dark matter halos as a function of halo mass. For this we need to identify the dark matter halos from the output particle distribution of the N-body simulations, and this determination is performed using a modified version of MHF (Knebe & Gibson 2004), MLAPM's default halo finder.

MHF optimally utilizes the refinement structure of the simulation grids to pin down the regions in which potential halos reside and organize the refinement hierarchy into a tree structure. MLAPM refines grids according to the particle density on them and so the boundaries of the refinements are simply isodensity contours. MHF collects the particles within these isodensity contours (as well as some particles outside). It then performs the following operations: (1) assuming spherical symmetry of the halo, calculate the escape velocity v_{esc} at the position of each particle, (2) if the velocity of the particle exceeds v_{esc} then it does not belong to the virialized halo and is removed. Steps (1) and (2) are then iterated until all unbound particles are removed from the halo or the number of particles in the halo falls below a pre-defined threshold, which is 20 in our simulations. Note

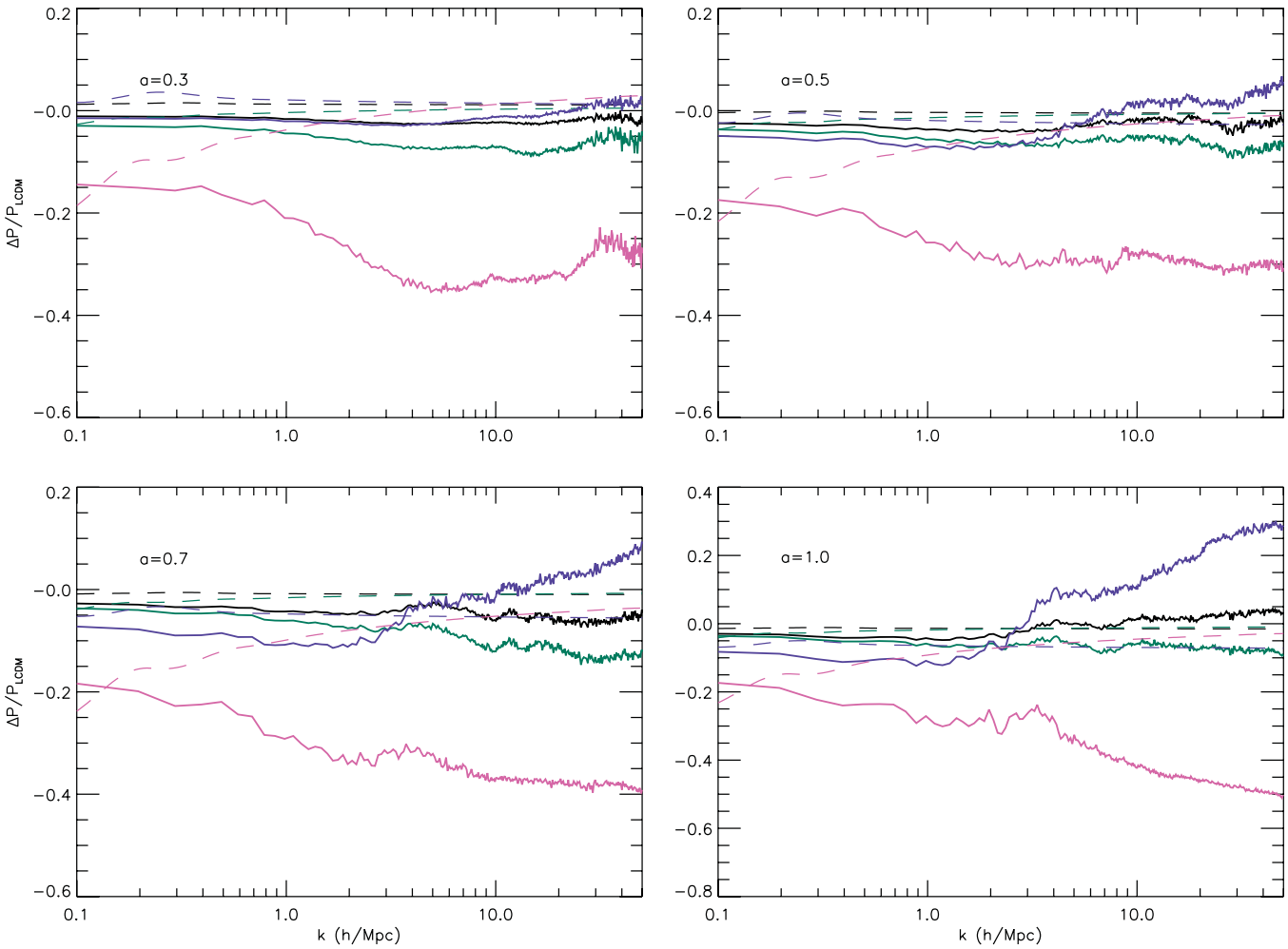

Figure 5. Fractional difference between the nonlinear power spectra for the extended quintessential and ΛCDM models. The results for the four models of $(\alpha, \gamma) = (0.1, -0.2)$, $(0.1, 0.2)$, $(0.5, -0.2)$, and $(0.5, 0.2)$ are, respectively, represented by the black, green, purple, and pink curves. The four panels are for four output times $a = 0.3, 0.5, 0.7$, and 1.0, as indicated inside the corresponding frames. The solid and dashed curves are, respectively, the results from N-body simulations and linear perturbation computation.

(A color version of this figure is available in the online journal.)

that the removal of unbound particles is not used in some halo finders using the spherical overdensity (SO) algorithm, which includes the particles in the halo as long as they are within the radius of a virial density contrast. Another advantage of MHF is that it does not require a predefined linking length in finding halos, such as the friend-of-friend procedure.

Our modification to MHF is simple: because the effective gravitational constant in the extended quintessence models is rescaled by a factor $G_{\rm N}$ (cf. Equation (34)), the escape velocity of particles from a halo is also multiplied by this factor, and in MHF we have only changed the criterion for removing particles from virialized halos accordingly. In reality, because we are only interested in the $a = 1$ halos in this work, $G_{\rm N}$ is quite close to 1 and the effect of our modification is not large.

The mass functions for our simulated models are shown in Figure 6. It shows that all extended quintessence models considered here, irrespective of their parameters, produce less massive halos than ΛCDM, whereas only the model $(\alpha, \gamma) = (0.5, -0.2)$ produces a larger number of less massive halos. These features are in broad agreement with those shown in the matter power spectra (Figure 5), where all models show less matter clustering on the large scales, whereas only the model $(\alpha, \gamma) = (0.5, -0.2)$ shows more power on small scales. The physical reason is again the competition between the modified background expansion rate and rescaled effective gravitational constant $G_{\rm N}$.

4.4. Halo Properties

In the ΛCDM paradigm, it is well known that the internal density profiles of dark matter halos are very well described by the Navarro–Frenk–White (NFW; Navarro et al. 1996) formalism

$$\frac{\rho(r)}{\rho_c} = \frac{\beta}{\frac{r}{R_s}\left(1 + \frac{r}{R_s}\right)^2}, \tag{37}$$

where ρ_c is the critical density for matter, β is a dimensionless fitting parameter, and R_s a second fitting parameter with length dimension. β and R_s are generally different for different halos and should be fitted for individual halos, but the formula (Equation (37)) is approximately universal.

We are thus interested in whether the halo profiles in an extended quintessential universe are also featured by this universal form. For this we select the 80 most massive halos from each simulation and fit their density profiles to Equation (37) using the method outlined by Jing (2000). The results show that the

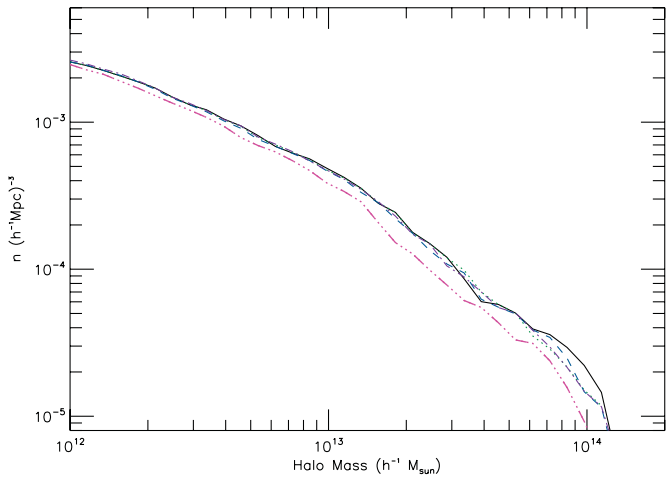

Figure 6. Mass functions for the models considered. The black solid, green-dotted, blue-dashed, purple dot-dashed, and pink dot-dot-dot-dashed curves stand for the results for ΛCDM and extended quintessence models with $(\alpha, \gamma) = (0.1, -0.2)$, $(0.1, 0.2)$, $(0.5, -0.2)$, and $(0.5, 0.2)$, respectively. The horizontal axis denotes the halo mass (in unit of $h^{-1}\,M_\odot$) and the vertical axis is the halo number density (in unit of $h^3\,\mathrm{Mpc}^{-3}$). Only the results at $a = 1$ are plotted.

(A color version of this figure is available in the online journal.)

NFW profile describes the extended quintessential halos at least as well as it does for the ΛCDM halos. Figure 7 shows the fittings for two halos randomly picked out of the 80: one at $\sim(10.34, 28.63, 13.91)\,h^{-1}$ Mpc with mass $\sim 1.88 \times 10^{14}\,M_\odot$ and the other at $(41.77, 31.91, 21.20)\,h^{-1}$ Mpc with a mass $\sim 4.98 \times 10^{13}\,M_\odot$. (Because we use the same initial conditions for all simulations, we are able to choose the halos such that they are the same halos in different simulations, e.g., they are at roughly the same position and share the most particles. We then fit all the halos we have selected explicitly to the NFW formula.)

There are some interesting features in Figure 7. First, for the models with $\alpha = 0.1$ (the top panels) the halo density profile for extended quintessence models (green asterisks) is very similar to the ΛCDM results (black crosses) and thus their fittings almost coincide. Second, for the model of $(\alpha, \gamma) = (0.5, -0.2)$, the chosen halos show more concentration of the density profiles in the scalar model than in ΛCDM. Third, the model of $(\alpha, \gamma) = (0.5, -0.2)$ has just the opposite trend and suffers a suppression of density in large parts of chosen halos.

To verify that the above features are actually typical for the corresponding models, we have plotted in Figure 8 the fitting results for all the 80 massive halos in all simulated models. Here, in addition to the NFW concentration parameter

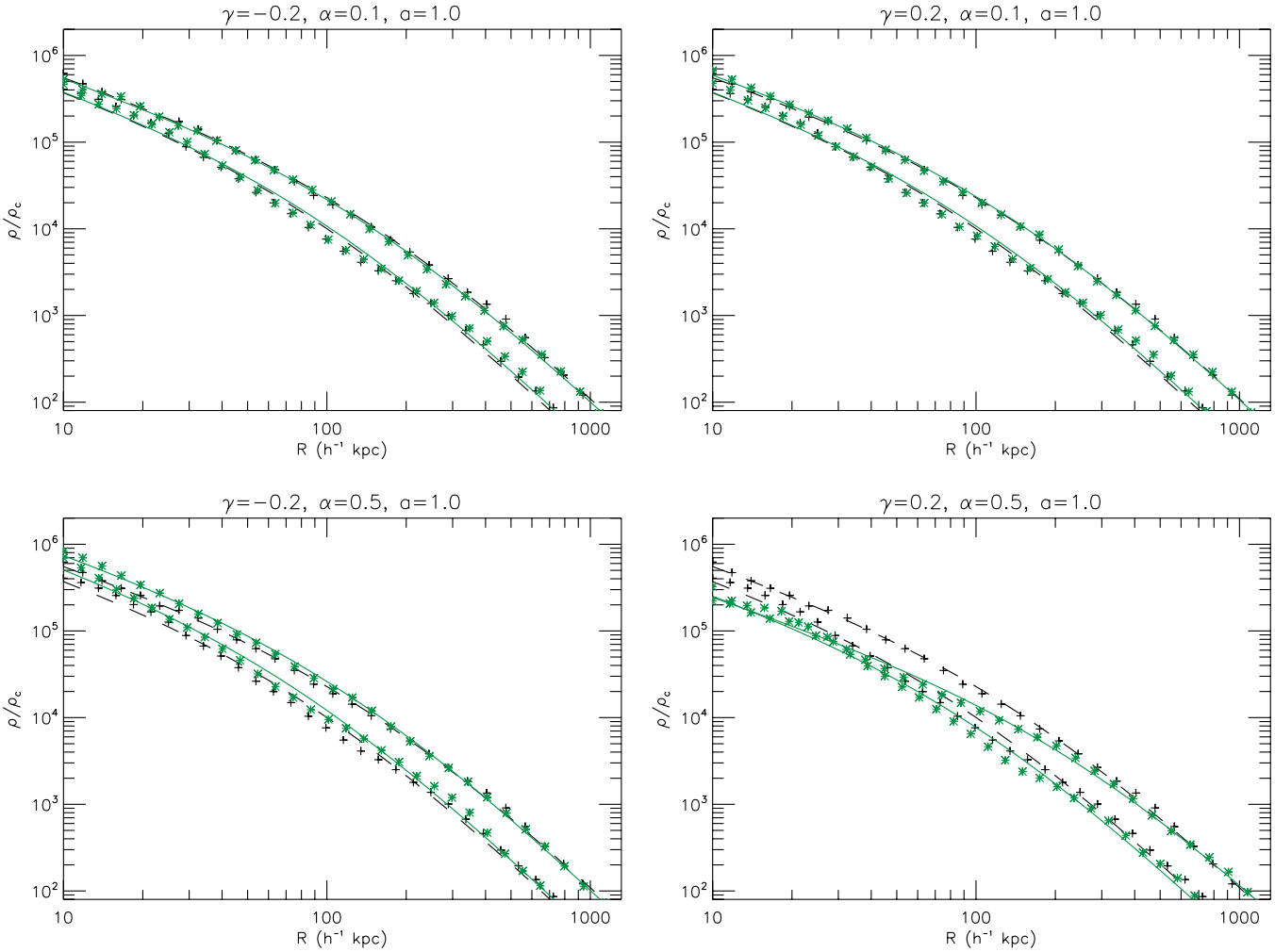

Figure 7. NFW fitting results for two halos randomly selected from the 80 most massive halos in each simulation (see the text for details). The upper and lower green asterisks represent, respectively, the density profile from *N*-body simulation for the more and less massive halos, and the green solid curves represent their NFW fittings. For comparison, we also show the corresponding *N*-body (black crosses) and fitting (black dashed curves) results for the ΛCDM model. The horizontal axis is the distance from halo center (in units of h^{-1} kpc) and the vertical axis is the density contrast. The four panels are for the four models as indicated above the frames.

(A color version of this figure is available in the online journal.)

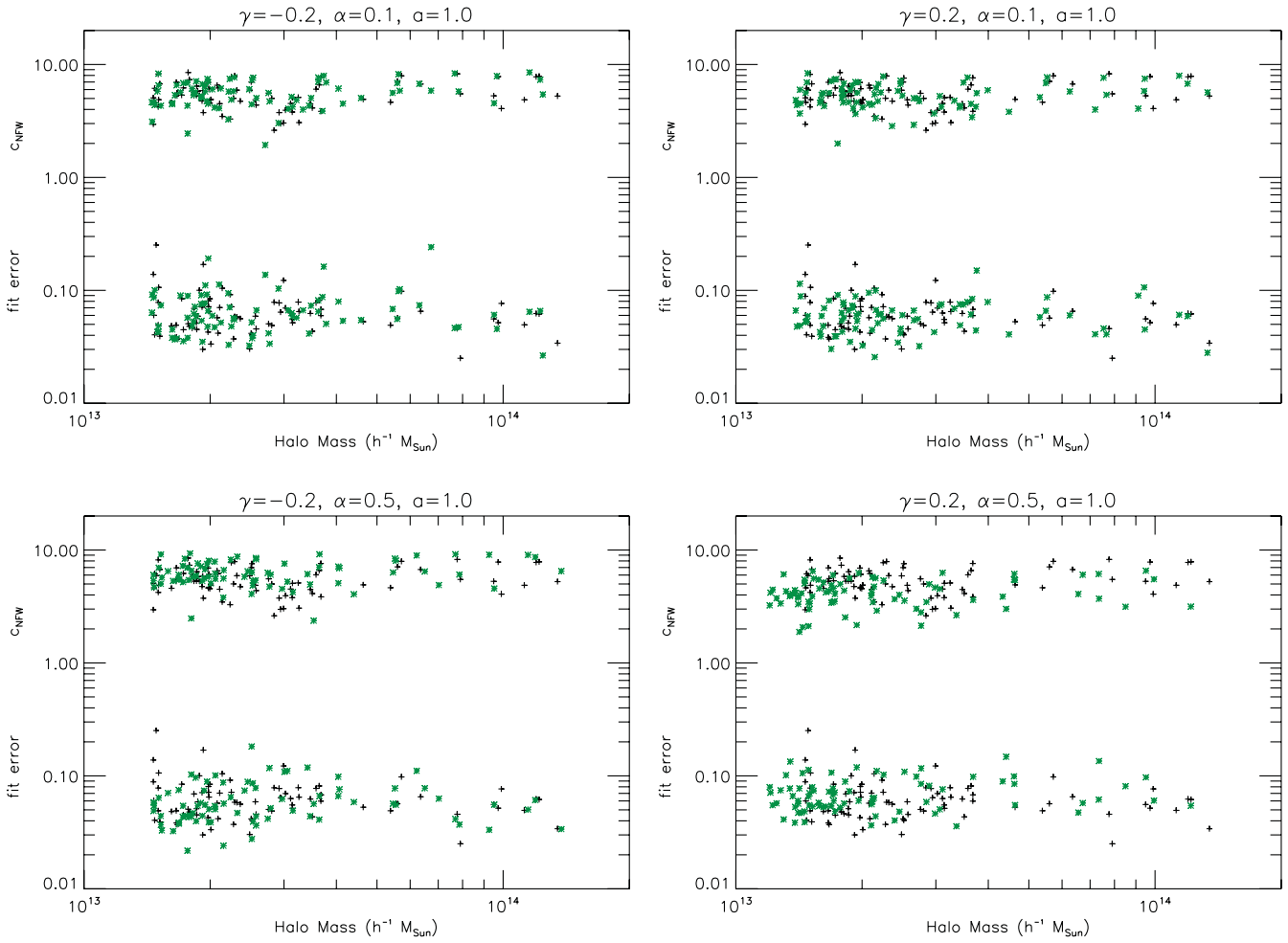

Figure 8. Scatter plot of the NFW fitting of the dark matter halo density profiles for the 80 most massive halos in each simulation box. In all panels, the black crosses and green asterisks represent the results of the ΛCDM and extended quintessence models, respectively. The upper cluster of points in each panel represents the fitted $c_{\rm NFW}$ and the lower cluster is for the fitting error, as indicated beside the vertical axis. The horizontal axis is the halo mass (in units of $h^{-1}\,M_{\odot}$). The four panels are for the models as indicated above the frames.

(A color version of this figure is available in the online journal.)

$c_{\rm NFW} = r_{200}/R_s$, where r_{200} is the radius at which the density is equal to 200 times the critical density ρ_c and R_s the NFW parameter, we have also shown the fitting errors for each halo.

We would like to point out several important implications of Figure 8. First, for all models the fitting error for the extended quintessential halos (lower green asterisks) is comparable to that for the ΛCDM halos (lower black crosses), indicating that the density profiles for the former are equally well described by the NFW formula (Equation (37)). Second, for the models with $\alpha = 0.1$ (the top panels) we can see that the fitted $c_{\rm NFW}$ for the extended quintessential halos is comparable to that for ΛCDM, which is in agreement with our finding in Figure 7 that the density profiles for the chosen halos are almost the same as in the ΛCDM prediction. Third, for the model of $(\alpha, \gamma) = (0.5, -0.2)$, the halos tend to be *more* concentrated (i.e., with *larger* $c_{\rm NFW}$) than in ΛCDM. Fourth, for the model $(\alpha, \gamma) = (0.5, 0.2)$, the halos tend to be *less* concentrated (i.e., with *smaller* $c_{\rm NFW}$) than in ΛCDM. The above three features show that our qualitative findings in Figure 7 are quite typical. Finally, the halo masses in the model of $(\alpha, \gamma) = (0.5, -0.2)$ are on average smaller than those in ΛCDM, because the upper green asterisks in the lower right panel consistently shift leftward with respect to the upper black crosses: this is consistent with the mass function result that this model produces fewer massive halos than ΛCDM.

The facts that the models $(\alpha, \gamma) = (0.5, 0.2)$ and $(\alpha, \gamma) = (0.5, -0.2)$ predict, respectively, lower and higher $c_{\rm NFW}$ than ΛCDM can be understood qualitatively. Let us suppose the effective gravitational constant $G_{\rm N}$ is $(1 + \beta)$ times as large as the bare G in ΛCDM. Then, on one hand, this means that the gravitational potential in the extended quintessence model is $(1 + \beta)$ times as deep as that in ΛCDM. On the other hand, the gravitational force and thus the accelerations and speeds of particles should also be rescaled by $(1 + \beta)$, which means that the kinetic energy of particles in extended quintessence models is $(1 + \beta)$ times that in ΛCDM. If $\beta > 0$, then the increase in kinetic energy is larger than that in the magnitude of the potential energy, which means that particles tend to escape from the halo center, thus producing a lower concentration $c_{\rm NFW}$, as is in the case of model $(\alpha, \gamma) = (0.5, 0.2)$. If $\beta < 0$, then the decrease in kinetic energy is larger than that in the magnitude of the potential energy, which means that particles tend to fall toward the halo center, thus producing a higher concentration $c_{\rm NFW}$, as is in the case of model $(\alpha, \gamma) = (0.5, -0.2)$. Such argument has been used in Li & Zhao (2010), Li & Barrow (2011), and Zhao et al. (2010a) for other models, and seems to give good qualitative explanations of the numerical results.

In summary, the halo density profiles for the extended quintessence models are well described by the NFW formula,

but the existence of the scalar field and in particular its coupling to curvature do change the concentration parameters of the halos, as long as the potential is not too flat. It seems that the modified background expansion rate exceeds the effect of the rescaled effective gravitational constant here.

4.5. Halo Profile for Scalar Field Perturbation

We have already seen that the coupling between the scalar field and the curvature scalar causes time and spatial variations of the locally measured gravitational constant $\kappa_\oplus$. It is then of interest to us to ask how $\kappa_\oplus$ varies across a given halo and whether this could produce observable effects. This subsection answers this question by giving an analytical formula and comparing it with numerical results.

Recall that Figure 3 shows that to a high precision the scalar field perturbation $a\sqrt{\kappa_*}\delta\varphi$ is proportional to the gravitational potential Φ (cf. Equation (35)) everywhere. This means that if we could derive an analytical formula for Φ in halos, then we know $a\sqrt{\kappa_*}\delta\varphi$ straightforwardly. Such a derivation has been done in Li et al. (2011) for a different model, but here we shall briefly repeat it for the extended quintessence model for completeness.

Assuming Equation (37) as the density profile and sphericity of halos, we can derive $V_c(r)$, the circular velocity of a particle moving around the halo at a distance r from halo center, to be

$$V_c^2(r) = \frac{GM(r)}{r} = 4\pi G\beta\rho_c R_s^3\left[\frac{1}{r}\ln\left(1+\frac{r}{R_s}\right)-\frac{1}{R_s+r}\right], \quad (38)$$

where $M(r)$ is the mass enclosed in radius r, G is the properly rescaled gravitational constant, namely, the $G_{\rm N}$ defined in Equation (34) that governs the local Cavendish-type experiments. Again, this equation is parameterized by β and R_s. From a simulation point of view, it is straightforward to measure $M(r)$ and then use Equation (38), instead of Equation (37), to fit the values of β and R_s; from an observational viewpoint, it is easy to measure $V_c(r)$, which could again be used to fit β and R_s.

The potential inside a spherical halo is then given as

$$\Phi(r) = \int_0^r \frac{GM(r')}{r'^2}dr' + C, \quad (39)$$

in which $GM(r)/r^2$ is the gravitational force and C is a constant to be fixed using the fact that $\Phi(r=\infty)=\Phi_\infty$, where Φ_∞ is the value of the potential far from the halo.

Using the formula for $GM(r)/r^2$ given in Equation (38) it is not difficult to find that

$$\int_0^r \frac{GM(r')}{r'^2}dr' = 4\pi G\beta\rho_c R_s^3\left[\frac{1}{R_s}-\frac{\ln\left(1+\frac{r}{R_s}\right)}{r}\right]$$

and so

$$C = \Phi_\infty - 4\pi G\beta\rho_c R_s^2. \quad (40)$$

Then it follows that

$$\Phi(r) = \Phi_\infty - 4\pi G\beta\rho_c\frac{R_s^3}{r}\ln\left(1+\frac{r}{R_s}\right). \quad (41)$$

If the halo is *isolated*, then $\Phi_\infty = 0$ and we get

$$\Phi(r) = -4\pi G\beta\rho_c\frac{R_s^3}{r}\ln\left(1+\frac{r}{R_s}\right). \quad (42)$$

However, in N-body simulations, we have a large number of dark matter halos and no halo is totally isolated from the others. In such situations, Φ_∞ in Equation (41) should be replaced by Φ_*, which is the potential produced by other halos inside the considered halo (note that in practice Φ_* could be position dependent as well, but for simplicity we assume that it is a constant, which is a good assumption for many halos). Then we get

$$a\sqrt{\kappa}\delta\varphi(r) = -\frac{2\gamma\sqrt{\kappa_*}\bar{\varphi}}{1+\frac{8\gamma^2\kappa_*\bar{\varphi}}{1+\gamma\kappa_*\bar{\varphi}}} \times\left[\Phi_* - 4\pi G\beta\rho_c\frac{R_s^3}{r}\ln\left(1+\frac{r}{R_s}\right)\right]. \quad (43)$$

Equation (43) provides a neat analytical formula for $a\sqrt{\kappa}\delta\varphi$ in halos, but unfortunately in most cases it cannot be used directly because we lack information about Φ_*. We will then be forced either to fit Φ_* as a free parameter, or tune its value to match simulations or observations. In this work, we take the second approach, and we find that with an appropriate value of Φ_* and with values of β and R_s fitted using Equation (38), Equation (43) agrees with numerical results for most halos.

Some examples are shown in Figure 9, in which we have computed $a\sqrt{\kappa}\delta\varphi(r)$ using four different methods: direct N-body simulation results (large green crosses), Equation (43) with $\Phi_* = 0$ (solid curves), Equation (43) with Φ_* properly tuned (dashed curves), and Equation (35) with Φ directly from N-body simulations (small red asterisks). Clearly the crosses and asterisks agree with each other very well, which is another demonstration that Equation (35) is a very good approximation (cf. Figure 3). The solid curves differ significantly from the numerical results, showing that Φ_* is actually nonzero; once it is appropriately tuned, then Equation (43) (dashed curves) agrees with the numerical results very well for all the chosen halos. Equation (43) therefore provides a useful analytical formula that might aid in general analysis.

We also note that across the halos the variation of $a\sqrt{\kappa}\delta\varphi$ is typically $\lesssim\mathcal{O}\left(10^{-6}\sim10^{-5}\right)$. Such a small variation is unlikely to be detectable using current observational instruments, and thus we do not expect special constraints based on the spatial variation of G. However, we stress that the above result is only for a class of extended quintessence models, and although we expect it to be valid for other potentials that are not particularly nonlinear, the situation could be dramatically changed in cases where the potential or coupling function becomes highly nonlinear. Such models require a more careful treatment, and some of the approximations adopted above become invalid, and are thus beyond the scope of the current work.

5. SUMMARY AND CONCLUSION

In summary, in this paper we have described a numerical method to study extended quintessence models, where the quintessence field has a scalar–tensor type of coupling to the curvature, from background cosmology to nonlinear structure formation, and discussed the regime of validity of the method. Instead of assuming a Yukawa force due to scalar coupling or simply a rescaling of the gravitational constant, we have solved the scalar field and its spatial variation explicitly from their equation of motion. This is a necessary step in general to obtain reliable results and to check various approximations that are made to simplify the computation.

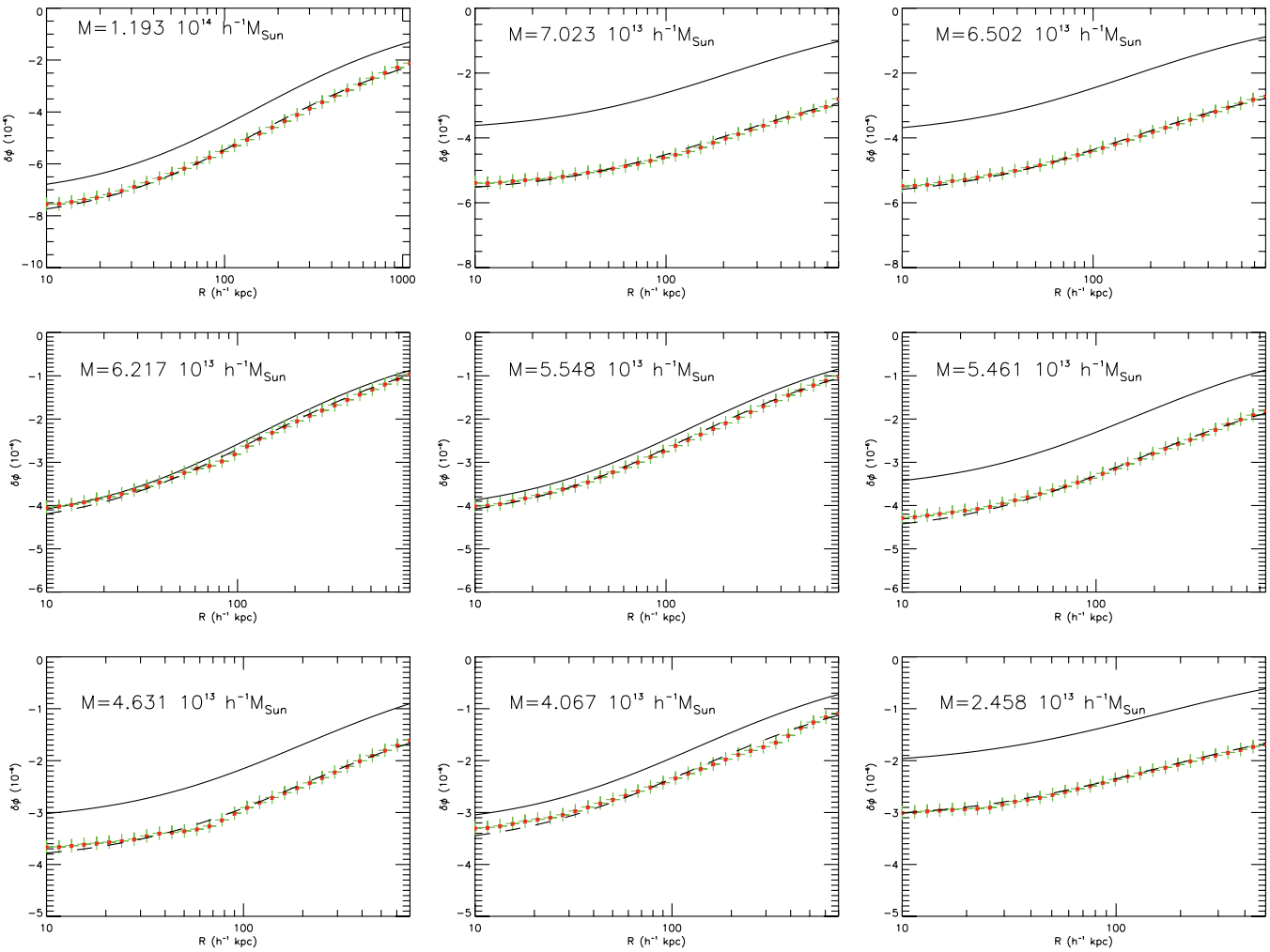

Figure 9. Comparison between our analytic formula for the scalar field perturbation $a\sqrt{\kappa_*}\delta\varphi$ (Equation (43)) and the results from numerical simulation. The nine panels are for nine halos selected from the simulation box, whose masses are indicated inside each frame. In each panel, the solid curve is Equation (43) with $\Phi_* = 0$, green crosses are the numerical results for $a\sqrt{\kappa_*}\delta\varphi$, the dashed curve is Equation (43) with Φ_* appropriately tuned to match the green crosses, and the red asterisks are the $a\sqrt{\kappa_*}\delta\varphi$ computed from the value of Φ using Equation (35). The horizontal axis is the distance from the halo center, and vertical axis stands for the value of $a\sqrt{\kappa_*}\delta\varphi$.

(A color version of this figure is available in the online journal.)

As specific examples, we apply the above method to a specific class of models with inverse power-law potential (Equation (10)) and non-minimal coupling (Equation (11)). The analysis of the background cosmology and its linear perturbation shows that for these models the effective gravitational "constants" relevant for the cosmic expansion rate and structure formation are either both increased or both decreased (albeit by slightly different amounts). The two effects compete and cancel each other, and as a result the net effect on large-scale structure in the linear regime is weak (cf. Figure 2). We then investigated whether a more significant signature of the scalar field could be imprinted in the nonlinear regime of structure formation.

The nonlinear matter power spectra plotted in Figure 5 suggests that the effect of the scalar field is more significant in the nonlinear regime. For the models with $\alpha = 0.5$ (i.e., steeper potential), the scalar field changes (either increases or decreases) the matter power spectrum by 30% $\sim$ 50% on small scales with respect to the ΛCDM prediction. Going to nonlinear scales thus greatly enhances the power of constraining such models using cosmological data. However, the power is more limited for models with $\alpha = 0.1$ (i.e., shallower potential); their matter power spectra are very similar to the ΛCDM results. Of the two competing effects mentioned above, we find that the modified background expansion rate is more influential on nonlinear scales.

Properties of mass functions (cf. Figure 6) are in qualitative agreement with what we have seen in the matter power spectrum, with the extended quintessence models producing fewer massive halos than ΛCDM. Therefore, galaxy cluster counts could place meaningful constraints on such models as well. But as with the matter power spectrum, the mass function for the models with $\alpha = 0.1$ (i.e., shallower potential) is very similar to the ΛCDM result.

The halo density profiles for the extended quintessence models are shown to be well described by the well-known NFW formula (cf. Figures 7 and 8). In Figure 8, we have shown the results of the fitting for the 80 most massive halos from each simulation. Consistent with the findings in Figures 5 and 6, we see that the concentration parameter $c_{\rm NFW}$ for the halos in the $\alpha = 0.1$ models is almost the same as for the ΛCDM halos. But for $\alpha = 0.5$, the $\gamma = -0.2$ and $\gamma = 0.2$ cases predict overall larger and smaller $c_{\rm NFW}$ than ΛCDM, respectively. Furthermore, Figure 8 clearly shows that the halos in the $(\alpha, \gamma) = (0.5, 0.2)$ model are consistently less massive

than those in ΛCDM, as suggested by the mass function plots.

Scalar–tensor theories (which the extended quintessence models belong to) are often studied in the context of a varying gravitational constant, and so we have also considered the spatial variations (time variation has been investigated in detail elsewhere and will not be repeated here) in the scalar field (or equivalently the locally measured gravitational constant $\kappa_\oplus$). We first showed in Figure 3 that the approximation that the scalar field perturbation $a\sqrt{\kappa_*}\delta\varphi$ is proportional to the gravitational potential Φ (cf. Equation (35)) is fairly accurate. Then, based on this fact and using the NFW density profile, we derive an analytical formula for $a\sqrt{\kappa_*}\delta\varphi(r)$ in spherical halos, in which the parameters are obtained by fitting the NFW circular velocity profile. We have shown that this formula could be tuned to fit the numerical results pretty well for most halos (cf. Figure 9).

Figure 9 indicates that the spatial variation of $a\sqrt{\kappa_*}\delta\varphi$ across halos is at most of order 10^{-5}, which is far smaller than the background value $\sqrt{\kappa_*}\bar{\varphi} \sim \mathcal{O}(0.1\text{–}1)$. Therefore, the spatial variation of $\kappa_\oplus$ is expected to be of order 10^{-5} or less in the halos, which is difficult to detect.

The smallness of $a\sqrt{\kappa_*}\delta\varphi$ also implies that the approximations we have made to simplify the simulations are valid. For example, because $|a\sqrt{\kappa_*}\delta\varphi| \ll 1$, which means it is reasonable to ignore the contribution from $\dot{\delta\varphi}, \ddot{\delta\varphi}$ to the total density/pressure perturbation, we can also replace φ by $\bar{\varphi}$ in the coefficients of perturbation quantities such as $\vec{\partial}^2_{\mathbf{x}}\Phi$ and $\vec{\partial}^2_{\mathbf{x}}(a\sqrt{\kappa_*}\delta\varphi)$. Moreover, the quasi-static limit, i.e., neglecting $\dot{\delta\varphi}, \ddot{\delta\varphi}$ compared to $\vec{\partial}^2_{\mathbf{x}}(a\sqrt{\kappa_*}\delta\varphi)$, is guaranteed to work well.

One of the most important results of this work is that it confirms explicitly that, for a broad range of extended quintessence models, the N-body simulation reduces to modifying the background expansion rate and rescaling the effective gravitational constant based on the background value of φ. This works to quite high accuracy and thus there is no need to solve the scalar field equation of motion explicitly, which is particularly time-consuming for large simulations. However, we expect this approximation to break down in extreme situations where the potential (or perhaps the coupling function) becomes highly nonlinear, and then both our results and method might have to be revised.

The work described in this paper has been performed on TITAN, the computing facilities at the University of Oslo in Norway; coding and testing are done on the SARA supercomputer in the Netherlands, supported by the European Community Research Infrastructure Action under the FP7 "Structuring the European Research Area" Programme. Postprocessing is done on COSMOS, the UK's National Cosmology Supercomputer. We have used POWMES (Colombi et al. 2008) to measure the matter power spectrum from output particle distribution, and a modified version of CAMB (Lewis et al. 2000) for our linear perturbation computation. We thank David Wands for discussions. B.L. is supported by the Research Fellowship at Queens' College, Cambridge, and the Science and Technology Facility Council of the United Kingdom. D.F.M. thanks the Research Council of Norway FRINAT grant 197251/V30.

APPENDIX A

USEFUL EXPRESSIONS

In this appendix, we list some useful expressions in the derivation of our equations, because different researchers use different conventions.

Our line element is

$$ds^2 = a^2(1+2\phi)d\tau^2 - a^2(1-2\psi)\gamma_{ij}dx^i dx^j, \tag{A1}$$

where τ is the conformal time, x^i is the comoving coordinate, and γ_{ij} the metric in the three-space (with i, j running over 1, 2, 3). The nonzero Christoffel symbols, up to first order in perturbation, are

$$\Gamma^0_{00} = \frac{a'}{a} + \phi', \qquad \Gamma^0_{0i} = \phi_{,i}$$

$$\Gamma^i_{0j} = \left(\frac{a'}{a} - \psi'\right)\delta^i{}_j, \qquad \Gamma^i_{00} = \phi^{,i}$$

$$\Gamma^0_{ij} = \frac{a'}{a}(1-2\phi-2\psi)\gamma_{ij} - \psi'\gamma_{ij}$$

$$\Gamma^i_{jk} = -\psi_{,k}\delta^i{}_j - \psi_{,j}\delta^i{}_k + \psi^{,i}\gamma_{jk}, \tag{A2}$$

where a comma denotes a partial derivative with respect to the comoving coordinate, and indices are raised and lowered by γ^{ij} and γ_{ij}, respectively. $' \equiv d/d\tau$.

The Ricci tensor is

$$R_{ab} = \Gamma^c_{ab,c} - \Gamma^c_{ac,b} + \Gamma^c_{cd}\Gamma^d_{ab} - \Gamma^d_{cb}\Gamma^c_{ad} \tag{A3}$$

and its components up to first order in perturbation are

$$R_{00} = \phi^{,i}_{i} - 3\left[\frac{a''}{a} - \left(\frac{a'}{a}\right)^2\right] + 3\psi'' + 3\frac{a'}{a}(\phi' + \psi'),$$

$$R_{0i} = 2\psi'_{,i} + 2\frac{a'}{a}\phi_{,i},$$

$$R_{ij} = -\psi''\gamma_{ij} - \frac{a'}{a}(\phi' + 5\psi')\gamma_{ij} - (\phi - \psi)_{,ij} + \left[\frac{a''}{a} + \left(\frac{a'}{a}\right)^2\right](1 - 2\phi - 2\psi)\gamma_{ij} + \psi^{,k}_{k}\gamma_{ij}.$$

The Ricci scalar R and relevant components of Einstein tensor $G_{ab} = R_{ab} - \frac{1}{2}g_{ab}R$ are

$$R = \frac{6}{a^2}\left[\psi'' - \frac{a''}{a}(1 - 2\phi) + \frac{a'}{a}(\phi' + 3\psi')\right] - \frac{1}{a^2}\left[4\psi^{,i}_{i} - 2\phi^{,i}_{i}\right], \tag{A4}$$

$$G^0_{\ 0} = \frac{3}{a^2}\left(\frac{a'}{a}\right)^2(1 - 2\phi) - \frac{6}{a^2}\frac{a'}{a}\psi' + \frac{2}{a^2}\psi^{,i}_{i}, \tag{A5}$$

$$G^i_{\ j} = \frac{1}{a^2}\left[-2\psi'' - 2\frac{a'}{a}(\phi' + 2\psi') - (\phi - \psi)^{,k}_{k}\right]\delta^i_{\ j} + \frac{1}{a^2}\left[2\frac{a''}{a} - \left(\frac{a'}{a}\right)^2\right](1 - 2\phi)\delta^i_{\ j} + \frac{1}{a^2}(\phi - \psi)^{,i}_{j}. \tag{A6}$$

APPENDIX B

DISCRETE EQUATIONS FOR THE *N*-BODY SIMULATIONS

In the MLAPM code, the Poisson equation (Equation (25)) is (and in our modified code the scalar field equation of motion Equation (20) will also be) solved on discretized grid points, so we must develop the discrete versions of Equations (20) and (25) to be implemented in the code. Before doing that, we note that Equations (20) and (25) are not independent but are coupled together, which could further complicate the solver. As a result, we should first decouple them by eliminating $\vec{\partial}^2_{\mathbf{x}}(a\sqrt{\kappa_*}\delta\varphi)$ ($\vec{\partial}^2_{\mathbf{x}}\Phi$) from the equation for Φ ($\delta\varphi$). This is easy to do and the resulting equations are, respectively,

$$\begin{aligned}\left[1 + \frac{6\gamma^2\kappa_*\bar{\varphi}^2}{1 + \gamma\kappa_*\bar{\varphi}^2}\right]c^2\vec{\partial}^2_{\mathbf{x}}(a\sqrt{\kappa_*}\delta\varphi) = {} & -6\gamma(\mathcal{H}' + \mathcal{H}^2)a\sqrt{\kappa_*}\delta\varphi - 3\alpha\lambda H_0^2 a^3\left[\frac{1}{(\sqrt{\kappa_*}\varphi)^\alpha} - \frac{1}{(\sqrt{\kappa_*}\bar{\varphi})^\alpha}\right] \\ & - 3\gamma\sqrt{\kappa_*}\bar{\varphi}\left(1 + \gamma\kappa_*\bar{\varphi}_0^2\right)\Omega_m H_0^2\left[\frac{\rho_c}{1 + \gamma\kappa_*\varphi^2} - \frac{1}{1 + \gamma\kappa_*\bar{\varphi}^2}\right] \\ & + 6\gamma\sqrt{\kappa_*}\bar{\varphi}\lambda H_0^2 a^3\left[\frac{1}{(1 + \gamma\kappa_*\varphi^2)(\sqrt{\kappa_*}\varphi)^\alpha} - \frac{1}{(1 + \gamma\kappa_*\bar{\varphi}^2)(\sqrt{\kappa_*}\bar{\varphi})^\alpha}\right] \\ & - 2\gamma\sqrt{\kappa_*}\bar{\varphi}a[(1 + 3\gamma)\kappa_*\bar{\varphi}'^2 + 3\gamma\kappa_*\bar{\varphi}\bar{\varphi}'']\left[\frac{1}{1 + \gamma\kappa_*\varphi^2} - \frac{1}{1 + \gamma\kappa_*\bar{\varphi}^2}\right]\end{aligned} \tag{B1}$$

for the scalar field, and

$$\begin{aligned}\frac{1 + \gamma\kappa_*\bar{\varphi}^2 + 6\gamma^2\kappa_*\bar{\varphi}^2}{1 + \gamma\kappa_*\bar{\varphi}^2 + 8\gamma^2\kappa_*\bar{\varphi}^2}\vec{\partial}^2_{\mathbf{x}}\Phi = {} & \frac{3}{2}\left(1 + \gamma\kappa_*\bar{\varphi}_0^2\right)\Omega_m H_0^2\left[\frac{\rho_c}{1 + \gamma\kappa_*\varphi^2} - \frac{1}{1 + \gamma\kappa_*\bar{\varphi}^2}\right] \\ & - 3\lambda H_0^2 a^3\left[\frac{1}{(1 + \gamma\kappa_*\varphi^2)(\sqrt{\kappa_*}\varphi)^\alpha} - \frac{1}{(1 + \gamma\kappa_*\bar{\varphi}^2)(\sqrt{\kappa_*}\bar{\varphi})^\alpha}\right] \\ & + a[(1 + 3\gamma)\kappa_*\bar{\varphi}'^2 + 3\gamma\kappa_*\bar{\varphi}\bar{\varphi}'']\left[\frac{1}{1 + \gamma\kappa_*\varphi^2} - \frac{1}{1 + \gamma\kappa_*\bar{\varphi}^2}\right] + \frac{6\gamma^2\sqrt{\kappa_*}\bar{\varphi}}{1 + \gamma\kappa_*\bar{\varphi}^2 + 8\gamma^2\kappa_*\bar{\varphi}^2}(\mathcal{H}' + \mathcal{H}^2)a\sqrt{\kappa_*}\delta\varphi \\ & + \frac{3\gamma\alpha\lambda\sqrt{\kappa_*}\bar{\varphi}}{1 + \gamma\kappa_*\bar{\varphi}^2 + 8\gamma^2\kappa_*\bar{\varphi}^2}H_0^2 a^3\left[\frac{1}{(\sqrt{\kappa_*}\varphi)^{1+\alpha}} - \frac{1}{(\sqrt{\kappa_*}\bar{\varphi})^{1+\alpha}}\right]\end{aligned} \tag{B2}$$

for the gravitational potential.

Introducing the variable u (cf. Section 2.3), the Poisson equation becomes

$$\frac{1+\gamma\kappa_*\bar{\varphi}^2+6\gamma^2\kappa_*\bar{\varphi}^2}{1+\gamma\kappa_*\bar{\varphi}^2+8\gamma^2\kappa_*\bar{\varphi}^2}\nabla^2\Phi_c \tag{B3}$$

$$\begin{aligned}
&= \frac{3}{2}\left(1+\gamma\kappa_*\bar{\varphi}_0^2\right)\Omega_m\left[\frac{\rho_c}{1+\gamma\left(\sqrt{\kappa_*}\bar{\varphi}+\frac{B^2H_0^2}{ac^2}u\right)^2}-\frac{1}{1+\gamma\kappa_*\bar{\varphi}^2}\right]\\
&\quad -3\lambda a^3\left[\frac{1}{1+\gamma\left(\sqrt{\kappa_*}\bar{\varphi}+\frac{B^2H_0^2}{ac^2}u\right)^2}\frac{1}{\left(\sqrt{\kappa_*}\bar{\varphi}+\frac{B^2H_0^2}{ac^2}u\right)^\alpha}-\frac{1}{1+\gamma\kappa_*\bar{\varphi}^2}\frac{1}{(\sqrt{\kappa_*}\bar{\varphi})^\alpha}\right]\\
&\quad +a\left[(1+3\gamma)\frac{\kappa_*\bar{\varphi}'^2}{H_0^2}+3\gamma\sqrt{\kappa}_*\bar{\varphi}\frac{\sqrt{\kappa_*}\bar{\varphi}''}{H_0^2}\right]\left[\frac{1}{1+\gamma\left(\sqrt{\kappa_*}\bar{\varphi}+\frac{B^2H_0^2}{ac^2}u\right)^2}-\frac{1}{1+\gamma\kappa_*\bar{\varphi}^2}\right]\\
&\quad +\frac{\gamma\sqrt{\kappa_*}\bar{\varphi}}{1+\gamma\kappa_*\varphi^2+8\gamma^2\kappa_*\varphi^2}\left\{6\gamma\left[\frac{\mathcal{H}'}{H_0^2}+\frac{\mathcal{H}^2}{H_0^2}\right]\frac{(BH_0)^2}{c^2}u+3\alpha\lambda a^3\left[\frac{1}{\left(\sqrt{\kappa_*}\bar{\varphi}+\frac{B^2H_0^2}{ac^2}u\right)^{1+\alpha}}-\frac{1}{(\sqrt{\kappa_*}\bar{\varphi})^{1+\alpha}}\right]\right\},
\end{aligned} \tag{B4}$$

where λ is defined in Section 2.3 and is a constant of $\mathcal{O}(1)$. We have also used the code unit for other quantities. This equation contains u, which must be solved from the scalar field equation of motion.

The scalar field equation of motion can be similarly written. In order that the equation can be integrated into MLAPM, we need to discretize it for the application of Newton–Gauss–Seidel relaxation method. This means writing down a discrete version of this equation on a uniform grid with grid spacing h. Suppose we want to achieve second-order precision, as is in the default Poisson solver of MLAPM, then $\nabla^2 u$ in one dimension can be written as

$$\nabla^2 u \to \nabla^{h2}u_j \;=\; \frac{u_{j+1}+u_{j-1}-2u_j}{h^2}, \tag{B5}$$

where a subscript $_j$ means that the quantity is evaluated on the jth point. The generalization to three dimensions is straightforward.

The discrete version of the equation of motion for u is then

$$L^h(u_{i,j,k})=0, \tag{B6}$$

in which

$$\begin{aligned}
L^h(u_{i,j,k}) &= \frac{1+\gamma\kappa_*\bar{\varphi}^2+6\gamma^2\kappa_*\bar{\varphi}^2}{1+\gamma\kappa_*\bar{\varphi}^2}\frac{1}{h^2}[u_{i+1,j,k}+u_{i-1,j,k}+u_{i,j+1,k}+u_{i,j-1,k}+u_{i,j,k+1}+u_{i,j,k-1}-6u_{i,j,k}]\\
&\quad +3\gamma\sqrt{\kappa_*}\bar{\varphi}\left(1+\gamma\kappa_*\bar{\varphi}_0^2\right)\Omega_m\left[\frac{\rho_c}{1+\gamma\left(\sqrt{\kappa_*}\bar{\varphi}+\frac{B^2H_0^2}{ac^2}u_{i,j,k}\right)^2}-\frac{1}{1+\gamma\kappa_*\bar{\varphi}^2}\right]\\
&\quad +3\alpha\lambda a^3\left[\frac{1}{\left(\sqrt{\kappa_*}\bar{\varphi}+\frac{B^2H_0^2}{ac^2}u_{i,j,k}\right)^{1+\alpha}}-\frac{1}{(\sqrt{\kappa_*}\bar{\varphi})^{1+\alpha}}\right]+6\gamma\frac{\mathcal{H}'+\mathcal{H}^2}{H_0^2}\frac{B^2H_0^2}{c^2}u_{i,j,k}\\
&\quad -6\gamma\sqrt{\kappa_*}\bar{\varphi}\lambda a^3\left[\frac{1}{1+\gamma\left(\sqrt{\kappa_*}\bar{\varphi}+\frac{B^2H_0^2}{ac^2}u_{i,j,k}\right)^2}\frac{1}{\left(\sqrt{\kappa_*}\bar{\varphi}+\frac{B^2H_0^2}{ac^2}u_{i,j,k}\right)^\alpha}-\frac{1}{1+\gamma\kappa_*\bar{\varphi}^2}\frac{1}{(\sqrt{\kappa_*}\bar{\varphi})^\alpha}\right]\\
&\quad +2\gamma\sqrt{\kappa_*}\bar{\varphi}a\left[(1+3\gamma)\frac{\kappa_*\bar{\varphi}'^2}{H_0^2}+3\gamma\sqrt{\kappa}_*\bar{\varphi}\frac{\sqrt{\kappa_*}\bar{\varphi}''}{H_0^2}\right]\left[\frac{1}{1+\gamma\left(\sqrt{\kappa_*}\bar{\varphi}+\frac{B^2H_0^2}{ac^2}u_{i,j,k}\right)^2}-\frac{1}{1+\gamma\kappa_*\bar{\varphi}^2}\right].
\end{aligned} \tag{B7}$$

Then, the Newton–Gauss–Seidel iteration says that we can obtain a new (and often more accurate) solution of u, $u^{\rm new}_{i,j,k}$, using our knowledge about the old (and less accurate) solution $u^{\rm old}_{i,j,k}$ via

$$u^{\rm new}_{i,j,k}=u^{\rm old}_{i,j,k}-\frac{L^h\left(u^{\rm old}_{i,j,k}\right)}{\partial L^h\left(u^{\rm old}_{i,j,k}\right)/\partial u_{i,j,k}}. \tag{B8}$$

The old solution will be replaced by the new solution to $u_{i,j,k}$ once the new solution is ready, using the red–black Gauss–Seidel sweeping scheme. Note that

$$\begin{aligned}\frac{\partial L^h(u_{i,j,k})}{\partial u_{i,j,k}} = & -\frac{1+\gamma\kappa_*\bar{\varphi}^2+6\gamma^2\kappa_*\bar{\varphi}^2}{1+\gamma\kappa_*\bar{\varphi}^2}\frac{6}{h^2}+6\gamma\frac{\mathcal{H}'+\mathcal{H}^2}{H_0^2}\frac{B^2H_0^2}{c^2}-\frac{3\alpha(1+\alpha)\lambda a^2\left(BH_0/c\right)^2}{\left(\sqrt{\kappa_*}\bar{\varphi}+\frac{B^2H_0^2}{ac^2}u_{i,j,k}\right)^{2+\alpha}}\\ & -6\gamma^2\frac{B^2H_0^2}{ac^2}\sqrt{\kappa_*}\bar{\varphi}\left(1+\gamma\kappa_*\bar{\varphi}_0^2\right)\Omega_m\rho_c\frac{\sqrt{\kappa_*}\bar{\varphi}+\frac{B^2H_0^2}{ac^2}u_{i,j,k}}{\left[1+\gamma\left(\sqrt{\kappa_*}\bar{\varphi}+\frac{B^2H_0^2}{ac^2}u_{i,j,k}\right)^2\right]^2}\\ & +12\gamma^2\frac{B^2H_0^2}{ac^2}\lambda\sqrt{\kappa_*}\bar{\varphi}a^3\frac{\sqrt{\kappa_*}\bar{\varphi}+\frac{B^2H_0^2}{ac^2}u_{i,j,k}}{\left[1+\gamma\left(\sqrt{\kappa_*}\bar{\varphi}+\frac{B^2H_0^2}{ac^2}u_{i,j,k}\right)^2\right]^2}\frac{1}{\left(\sqrt{\kappa_*}\bar{\varphi}+\frac{B^2H_0^2}{ac^2}u_{i,j,k}\right)^{\alpha}}\\ & +6\alpha\gamma\frac{B^2H_0^2}{ac^2}\lambda\sqrt{\kappa_*}\bar{\varphi}a^3\frac{1}{1+\gamma\left(\sqrt{\kappa_*}\bar{\varphi}+\frac{B^2H_0^2}{ac^2}u_{i,j,k}\right)^2}\frac{1}{\left(\sqrt{\kappa_*}\bar{\varphi}+\frac{B^2H_0^2}{ac^2}u_{i,j,k}\right)^{1+\alpha}}\\ & -4\gamma^2\frac{B^2H_0^2}{c^2}\sqrt{\kappa_*}\bar{\varphi}\left[(1+3\gamma)\frac{\kappa_*\bar{\varphi}'^2}{H_0^2}+3\gamma\sqrt{\kappa}_*\bar{\varphi}\frac{\sqrt{\kappa_*}\bar{\varphi}''}{H_0^2}\right]\frac{\sqrt{\kappa_*}\bar{\varphi}+\frac{B^2H_0^2}{ac^2}u_{i,j,k}}{\left[1+\gamma\left(\sqrt{\kappa_*}\bar{\varphi}+\frac{B^2H_0^2}{ac^2}u_{i,j,k}\right)^2\right]^2}. \end{aligned} \tag{B9}$$

In principle, if we start from a high redshift, then the initial guess of $u_{i,j,k}$ for the relaxation can be chosen so that the initial value of φ in all space is equal to the background value $\bar{\varphi}$, because at this time we expect this to be approximately true any way. At subsequent time steps we could use the solution for $u_{i,j,k}$ from the previous time step as our initial guess. If the time step is small enough then we would expect u to change only slightly between consecutive time steps so that such a guess will be good enough for the iterations to converge quickly.

APPENDIX C

ALGORITHM TO SOLVE THE BACKGROUND EVOLUTION

Here, we give our formulae and algorithm for the background field equations which can also be applied to linear Boltzmann codes such as CAMB. Throughout this appendix we use the conformal time τ instead of the physical time t, and $' \equiv d/d\tau$, $\mathcal{H} \equiv a'/a$. All quantities appearing here are background ones unless stated otherwise.

For convenience, we will work with dimensionless quantities and define $\psi \equiv \sqrt{\kappa_*}\varphi$ and $N \equiv \ln a$ so that

$$\psi' = \mathcal{H}\frac{d\psi}{dN}, \tag{C1}$$

$$\psi'' = \mathcal{H}^2\frac{d^2\psi}{dN^2}+\mathcal{H}'\frac{d\psi}{dN}. \tag{C2}$$

With these definitions it is straightforward to show that the scalar field equation of motion can be expressed as

$$\left(\frac{\mathcal{H}}{\mathcal{H}_0}\right)^2\frac{d^2\psi}{dN^2}+\left(2\frac{\mathcal{H}^2}{\mathcal{H}_0^2}+\frac{\mathcal{H}'}{\mathcal{H}_0^2}\right)\frac{d\psi}{dN}+\frac{\kappa_*}{\mathcal{H}_0^2}a^2\frac{\partial V(\psi)}{\partial\psi}-3\left(\frac{\mathcal{H}'}{\mathcal{H}_0^2}+\frac{\mathcal{H}^2}{\mathcal{H}_0^2}\right)\frac{\partial f(\psi)}{\partial\psi}=0, \tag{C3}$$

where $\mathcal{H}_0$ is the current value of $\mathcal{H}$.

Obviously, we need to know how to compute the quantities $\mathcal{H}/\mathcal{H}_0$ and $\mathcal{H}'/\mathcal{H}_0$ as well. For $\mathcal{H}/\mathcal{H}_0$, we start with the Friedmann equation

$$3\mathcal{H}^2 = \frac{1}{1+f}\kappa_*\left[\rho_m+\rho_r+V(\psi)\right]a^2+\frac{1}{1+f}\left[\frac{1}{2}\left(\frac{d\psi}{dN}\right)^2-3\frac{df}{d\psi}\frac{d\psi}{dN}\right]\mathcal{H}^2, \tag{C4}$$

where ρ_m and ρ_r are the energy densities for matter and radiation, respectively. We define the fractional energy densities for matter and radiation, respectively, as

$$\Omega_m \equiv \frac{\kappa_{\rm eff}\rho_{m0}}{3\mathcal{H}_0^2} = \frac{1}{1+f_0}\frac{\kappa_*\rho_{m0}}{3\mathcal{H}_0^2}, \tag{C5}$$

$$\Omega_r \equiv \frac{\kappa_{\oplus 0}\rho_{r0}}{3\mathcal{H}_0^2} = \frac{1}{1+f_0}\frac{2\left(1+f_0\right)+4\left(\frac{df}{d\psi}\right)_0^2}{2\left(1+f_0\right)+3\left(\frac{df}{d\psi}\right)_0^2}\frac{\kappa_*\rho_{r0}}{3\mathcal{H}_0^2}, \tag{C6}$$

where a subscript $_0$ means the present-day value. Note the difference between these definitions, which comes from the different treatments for radiation and matter in numerical codes such as CAMB. For radiation, e.g., photon, we know the present temperature of the CMB and thus its exact energy density ρ_{r0}, as well as the locally measured value of gravitational constant $\kappa_{\oplus 0}$ (which in scalar–tensor theories is in general different from κ_*) and current Hubble expansion rate $\mathcal{H}_0$, and so the definition Equation (C6) comes out naturally, where we have used the relation between κ_* and $\kappa_\oplus$.[6] For matter, the fractional energy density is to be interpreted from the cosmological observables such as CMB and large-scale structure, which are obviously different in ΛCDM and scalar–tensor theories; consequently, there is some freedom in defining it and we make it as in Equation (C5).

Then, remembering that

$$\rho_m \propto a^{-3}, \tag{C7}$$

$$\rho_r \propto a^{-4}, \tag{C8}$$

we have

$$\left(\frac{\mathcal{H}}{\mathcal{H}_0}\right)^2 = \frac{\frac{\kappa_*}{\kappa_{\oplus 0}}\Omega_r a^{-2} + (1+f_0)\,\Omega_m a^{-1} + \frac{\kappa_* V a^2}{3\mathcal{H}_0^2}}{1 + f + \frac{df}{d\psi}\frac{d\psi}{dN} - \frac{1}{6}\left(\frac{d\psi}{dN}\right)^2}, \tag{C9}$$

in which (where both κ_* and $\kappa_{\oplus 0}$are constants and $\kappa_{\oplus 0}$ is the present value of $\kappa_\oplus$)

$$\frac{\kappa_*}{\kappa_{\oplus 0}} = (1+f_0)\,\frac{2(1+f_0) + 3\left(\frac{df}{d\psi}\right)_0^2}{2(1+f_0) + 4\left(\frac{df}{d\psi}\right)_0^2}. \tag{C10}$$

For $\mathcal{H}'/\mathcal{H}_0$, we use the Raychaudhuri equation

$$\begin{aligned}\mathcal{H}' =& -\frac{1}{6}\kappa_*(\rho + 3p)\,a^2 \\ =& -\frac{1}{6}\frac{1}{1+f}\kappa_*[\rho_m + 2\rho_r - 2V(\psi)]\,a^2 - \frac{1}{6}\frac{1}{1+f}\left(2 + 3\frac{d^2 f}{d\psi^2}\right)\left(\frac{d\psi}{dN}\right)^2\mathcal{H}^2 \\ & -\frac{1}{2}\frac{1}{1+f}\frac{df}{d\psi}\left(\frac{d\psi}{dN}\mathcal{H}' + \frac{d^2\psi}{dN^2}\mathcal{H}^2\right).\end{aligned} \tag{C11}$$

As in the above, dividing this by $\mathcal{H}_0^2$ and rearranging, we obtain

$$\frac{\mathcal{H}'}{\mathcal{H}_0^2} = -\frac{\frac{1}{2}\left[(1+f_0)\,\Omega_m a^{-1} + 2\frac{\kappa_*}{\kappa_{\oplus 0}}\Omega_r a^{-2}\right] - \frac{\kappa_* V a^2}{3\mathcal{H}_0^2}}{1 + f + \frac{1}{2}\frac{df}{d\psi}\frac{d\psi}{dN}} - \frac{\frac{1}{2}\frac{df}{d\psi}\frac{d^2\psi}{dN^2} + \left(\frac{1}{3} + \frac{1}{2}\frac{d^2 f}{d\psi^2}\right)\left(\frac{d\psi}{dN}\right)^2}{1 + f + \frac{1}{2}\frac{df}{d\psi}\frac{d\psi}{dN}}\frac{\mathcal{H}^2}{\mathcal{H}_0^2}. \tag{C12}$$

Substituting Equations (C9) and (C12) into Equation (C3), we finally arrive at

$$\frac{1 + f + \frac{3}{2}\left(\frac{df}{d\psi}\right)^2}{1 + f + \frac{1}{2}\frac{df}{d\psi}\frac{d\psi}{dN}}A\frac{d^2\psi}{dN^2} + (2A + B)\frac{d\psi}{dN} + \frac{\kappa_*}{\mathcal{H}_0^2}\frac{dV}{d\psi}a^2 - 3(A+B)\frac{df}{d\psi} = 0, \tag{C13}$$

in which we have defined

$$A \equiv \frac{\mathcal{H}^2}{\mathcal{H}_0^2}, \tag{C14}$$

$$B \equiv \frac{\mathcal{H}'}{\mathcal{H}_0^2} + \frac{\frac{1}{2}\frac{df}{d\psi}\frac{\mathcal{H}^2}{\mathcal{H}_0^2}}{1 + f + \frac{1}{2}\frac{df}{d\psi}\frac{d\psi}{dN}}\frac{d^2\psi}{dN^2}, \tag{C15}$$

where A and B do not contain $d^2\psi/dN^2$, to lighten the notation.

When solving for φ (or ψ), we just use Equation (C3) aided by Equations (C9) and (C12). It may appear then that, given any initial values for $\psi_{\rm ini}$ and $(d\psi/dN)_{\rm ini}$, the evolution of φ is obtainable. However, Equation (C9) is not necessarily satisfied for ψ evolved

[6] (Massless) neutrinos are treated similarly, but the neutrino background has a temperature lower than that of CMB, due to the energy transfer into photons during the electron–positron annihilation, but not into neutrinos that have decoupled by then.

in such way. Instead, it constrains the initial condition ψ must start with, and the way it must subsequently evolve. This in turn is determined by the parameters λ, α, γ, since α, γ specify a model and are fixed once the model is chosen; the only concern is λ.

As for the initial conditions $\psi_{\rm ini}$ and $(d\psi/dN)_{\rm ini}$, we have found that the subsequent evolution of ψ is rather insensitive to them. Thus, we choose $\psi_{\rm ini} = (d\psi/dN)_{\rm ini} = 0$ at some very early time (say $N_{\rm ini}$ corresponds to $a_{\rm ini} = e^{N_{\rm ini}} = 10^{-8}$) in all the models. Such a choice is clearly not only practical but also reasonable, given the fact that we expect that the scalar field starts high up the potential and rolls down subsequently.

As for λ, we use a trial-and-error method to find its value which ensures that (again subscript $_0$ indicates the current time)

$$\frac{\frac{\kappa_*}{\kappa_{\oplus 0}}\Omega_r + (1+f_0)\,\Omega_m + \frac{\kappa_* V_0}{3\mathcal{H}_0^2}}{1 + f_0 + \left(\frac{df}{d\psi}\right)_0\left(\frac{d\psi}{dN}\right)_0 - \frac{1}{6}\left(\frac{d\psi}{dN}\right)_0^2} = 1, \tag{C16}$$

which comes from setting $a = 1$ in Equation (C9).

We determine the correct value of λ for any given α, γ in this way using a trial-and-error routine, and then compute the values of ψ and $d\psi/dN$ for predefined values of N stored in an array. Their values at any time are then obtained using interpolation, and with these it is straightforward to compute other relevant quantities, such as $\mathcal{H}$, $\mathcal{H}'$, and φ, which are used in the linear perturbation computations.

REFERENCES

Amendola, L. 2000, Phys. Rev. D, 62, 043511
Amendola, L. 2004, Phys. Rev. D, 69, 103524
Angulo, R. E., & White, S. D. M. 2010, MNRAS, 405, 143
Baccigalupi, C., & Perrotta, F. 2000, MNRAS, 314, 1
Baccigalupi, C., Perrotta, F., & Matarrese, S. 2000, Phys. Rev. D, 61, 023507
Baldi, M. 2010, arXiv:1005.2188
Baldi, M., & Pettorino, V. 2010, arXiv:1006.3761
Baldi, M., Pettorino, V., Robbers, G., & Springel, V. 2010, MNRAS, 403, 1684
Barrow, J. D., & Shaw, D. J. 2010, arXiv:1007.3086
Bartolo, N., & Pietroni, M. 1999, Phys. Rev. D, 61, 023518
Bean, R. 2001, Phys. Rev. D, 64, 123516
Bean, R., Flanagan, E. E., Laszlo, I., & Trodden, M. 2008a, Phys. Rev. D, 78, 123514
Bean, R., Flanagan, E. E., & Trodden, M. 2008b, Phys. Rev. D, 78, 023009
Bean, R., & Magueijo, J. 2001, Phys. Lett. B, 517, 177
Boehmer, C. G., Caldera-Cabral, G., Chan, N., Lazkoz, R., & Maartens, R. 2010, Phys. Rev. D, 81, 083003
Boehmer, C. G., Caldera-Cabral, G., Lazkoz, R., & Maartens, R. 2008, Phys. Rev. D, 78, 023505
Brookfield, A. W., van de Bruck, C., Mota, D. F., & Tocchini-Valentini, D. 2006, Phys. Rev. Lett., 96, 061301
Caresia, P., Matarrese, S., & Moscardini, L. 2004, ApJ, 605, 21
Clifton, T., Mota, D. F., & Barrow, J. D. 2005, MNRAS, 358, 601
Colombi, S., Jaffe, A. H., Novikov, D., & Pichon, C. 2008, MNRAS, 393, 511
Copeland, E. J., Sami, M., & Tsujikawa, S. 2006, Int. J. Mod. Phys. D, 15, 1753
Damour, T., & Esposito-Farese, G. 1992, Class. Quantum Grav., 9, 2093
De Boni, C., Dolag, K., Ettori, S., Moscardini, L., Pettorino, V., & Baccigalupi, C. 2010, arXiv:1008.5376
Farrar, G. R., & Rosen, R. A. 2007, Phys. Rev. Lett., 98, 171302
Fujii, Y., & Maeda, K. 2003, The Scalar–Tensor Theory of Gravitation (Cambridge: Cambridge Univ. Press)
Hellwing, W. A., & Juszkiewicz, R. 2009, Phys. Rev. D, 80, 083522
Hellwing, W. A., Knollmann, S. R., & Knebe, A. 2010, MNRAS, 408, L104
Jennings, E., Baugh, C. M., Angulo, R. E., & Pascoli, S. 2010, MNRAS, 401, 2181
Jesus, J. F., Santos, R. C., Alcaniz, J. S., & Lima, J. A. S. 2008, Phys. Rev. D, 78, 063514
Jing, Y. P. 2000, ApJ, 535, 30
Kesden, M., & Kamionkowski, M. 2006a, Phys. Rev. Lett., 97, 131303
Kesden, M., & Kamionkowski, M. 2006b, Phys. Rev. D, 74, 083007
Keselman, J. A., Nusser, A., & Peebles, P. J. E. 2009, Phys. Rev. D, 80, 063517
Keselman, J. A., Nusser, A., & Peebles, P. J. E. 2010, Phys. Rev. D, 81, 063521
Knebe, A., & Gibson, B. K. 2004, MNRAS, 347, 1055
Knebe, A., Green, A., & Binney, J. 2001, MNRAS, 325, 845
Koivisto, T. 2005, Phys. Rev. D, 72, 043516
Koivisto, T., & Mota, D. F. 2007, Phys. Rev. D, 75, 023518
Lee, S., Liu, G.-C., & Ng, K.-W. 2006, Phys. Rev. D, 73, 083516
Lewis, A., Challinor, A., & Lasenby, A. 2000, ApJ, 538, 473
Li, B., & Barrow, J. D. 2011, Phys. Rev. D, in press (arXiv:1005.4231)
Li, B., Mota, D. F., & Barrow, J. D. 2011, ApJ, 728, 108
Li, B., & Zhao, H. 2009, Phys. Rev. D, 80, 044027
Li, B., & Zhao, H. 2010, Phys. Rev. D, 81, 104047
Maccio, A. V., Quercellini, C., Mainini, R., Amendola, L., & Bonometto, S. A. 2004, Phys. Rev. D, 69, 123516
Manera, M., & Mota, D. F. 2006, MNRAS, 371, 1373
Mangano, G., Miele, G., & Pettorino, V. 2003, Mod. Phys. Lett. A, 18, 831
Mota, D. F. 2008, J. Cosmol. Astropart. Phys., JCAP09(2008)006
Mota, D. F., Kristiansen, J. R., Koivisto, T., & Groeneboom, N. E. 2007, MNRAS, 382, 793
Mota, D. F., Pettorino, V., Robbers, G., & Wetterich, C. 2008a, Phys. Lett. B, 663, 160
Mota, D. F., & Shaw, D. J. 2006, Phys. Rev. Lett., 97, 151102
Mota, D. F., & Shaw, D. J. 2007, Phys. Rev. D, 75, 063501
Mota, D. F., Shaw, D. J., & Silk, J. 2008b, ApJ, 675, 29
Mota, D. F., & van de Bruck, C. 2004, A&A, 421, 71
Navarro, J. F., Frenk, C. S., & White, S. D. M. 1996, ApJ, 462, 563
Nunes, N. J., & Mota, D. F. 2006, MNRAS, 368, 751
Nusser, A., Gubser, S. S., & Peebles, P. J. E. 2005, Phys. Rev. D, 71, 083505
Perrotta, F., Baccigalupi, C., & Matarrese, S. 2000, Phys. Rev. D, 61, 023507
Pettorino, V., & Baccigalupi, C. 2008, Phys. Rev. D, 77, 103003
Pettorino, V., Baccigalupi, C., & Mangano, G. 2005, J. Cosmol. Astropart. Phys., JCAP01(2005)014
Press, W. H., Teukolsky, S. A., Vetterling, W. T., & Flannery, B. P. 1992, Numerical Recipes in C: The Art of Scientific Computing (2nd ed.; Cambridge: Cambridge Univ. Press)
Ratra, B., & Peebles, P. J. E. 1988, Phys. Rev. D, 37, 3406
Riazuelo, A., & Uzan, J.-P. 2002, Phys. Rev. D, 66, 023525
Rodriguez-Meza, M. A. 2008a, AIP Conf. Proc. 1083, Gravitation and Cosmology, ed. A. Herrera-Aguilar et al. (Melville, NY: AIP), 190
Rodriguez-Meza, M. A. 2008b, AIP Conf. Proc. 977, Recent Developments in Gravitation and Cosmology, ed. A. Macias, C. Laemmerzahl, & A. Camach (Melville, NY: AIP), 302
Rodriguez-Meza, M. A., Gonzalez-Morales, A. X., Gabbasov, R. F., & Cervantes-Cota, J. L. 2007, J. Phys.: Conf. Ser., 91, 012012
Saracco, F., Pietroni, M., Tetradis, N., Pettorino, V., & Robbers, G. 2010, Phys. Rev. D, 82, 023528
Schimd, C., Uzan, J.-P., & Riazuelo, A. 2005, Phys. Rev. D, 71, 083512
Shaw, D. J., & Mota, D. F. 2008, ApJS, 174, 277
Springel, V., & Farrar, G. 2007, MNRAS, 380, 911
Uzan, J.-P. 1999, Phys. Rev. D, 59, 123510
Uzan, J.-P. 2010, arXiv:1009.5514
Wang, L.-M., Caldwell, R. R., Ostriker, J. P., & Steinhardt, P. J. 2000, ApJ, 530, 17
Wintergerst, N., & Pettorino, V. 2010, Phys. Rev. D, 82, 103516
Zhao, G., Li, B., & Koyama, K. 2010a, arXiv:1011.1257
Zhao, H., Macció, A., Li, B., Hoekstra, H., & Feix, M. 2010b, ApJ, 712, L179
Zlatev, I., Wang, L.-M., & Steinhardt, P. J. 1999, Phys. Rev. Lett., 82, 896